Non-Adiabatic Interaction in CO_2^+ and the Effect of Hydration on Cation-π Interaction Between Benzene and Various Cations

Vikash Dhindhwal

A dissertation submitted for the partial fulfilment of

BS-MS dual degree in Science

Indian Institute of Science Education and Research Mohali

April 2014

Certificate of Examination

This is to certify that the dissertation titled "**Non-Adiabatic Interactions in CO_2^+ and the Effect of Hydration on the Cation-π interaction between Benzene and Different Cations**" submitted by **Mr. Vikash Dhindhwal** (Reg. No. MS09135) for the partial fulfilment of BS-MS dual degree programme of the Institute, has been examined by the thesis committee duly appointed by the Institute. The committee finds the work done by the candidate satisfactory and recommends that the report be accepted.

Dr. P. Balanarayan Dr. K. R. Shamasundar Professor N. Sathyamurthy (Supervisor)

Dated: April 25, 2014

Declaration

The work presented in this dissertation has been carried out by me under the guidance of Professor N. Sathyamurthy at the Indian Institute of Science Education and Research Mohali.

This work has not been submitted in part or in full for a degree, a diploma, or a fellowship to any other university or institute. Whenever contributions of others are involved, every effort is made to indicate this clearly, with due acknowledgement of collaborative research and discussions. This thesis is a bonafide record of original work done by me and all sources listed within have been detailed in the bibliography.

Vikash Dhindhwal

(Candidate)

Dated: April 25, 2014

In my capacity as the supervisor of the candidate's project work, I certify that the above statements by the candidate are true to the best of my knowledge.

Professor N. Sathyamurthy

(Supervisor)

Acknowledgement

I would like to express my sincere thanks and deep sense of gratitude to Professor N. Sathyamurthy for supervising my masters' project. He provided an excellent working environment. He is an excellent teacher and a great personality. His unique style of instruction and encouragement were the most important ingredients. It was my privilege to have association with him.

I am highly indebted to Professor Michael Baer, FHCMR The Hebrew University of Jerusalem, Israel, for supervising a part of my masters' thesis. I have learned a great deal of concepts from him. I have been immensely benefited by association with him.

I owe my thanks to Dr. Saurabh Srivastva, IIT Kanpur and Satyam Ravi, IISER Mohali, for discussions on the topics and providing me help during my project.

I am grateful to Sumit Mittal for helping me in the project.

I want to thank Agastya Bhati for discussions and providing a lively company during the project.

I also thank my thesis evaluation committee for their kind and useful suggestions to improve my thesis.

I would like to express my sincere thanks to my friends and colleagues at IISER Mohali for making my stay wonderful. I would like to extend my thanks to Harjit Sandhu, Deepak, Shivpal Kang, Saksham, Vidit, Yash, Uttam and Yatendra for their wonderful company.

I would like to thank Computer Centre, IISER Mohali for providing me the computing facility.

I would like to take this opportunity to thank all those who are not mentioned by name and helped me directly or indirectly during my project.

I owe my sincere thanks to my parents and my family for their constant support and encouragement during the project.

Last, but not the least, I thank Almighty without whom nothing is possible.

Vikash

List of Figures

List of Tables

Acronyms

ADT	Adiabatic-to-Diabatic Transformation
B-O	Born-Oppenheimer
JT CI	Jahn-Teller Conical Intersection
MP2	Møller-Plesset Perturbation
NACM	Non-Adiabatic Coupling Matrix
NACT	Non-Adiabatic Coupling Term
PEC	Potential Energy Curve
PES	Potential Energy Surface

Contents

Abstract

In Chapter 1, a study of the topological effects in CO_2^+ has been carried out by calculating non-adiabatic coupling terms (NACTs) between 1 ^{2}A', 2 ^{2}A' and 3 ^{2}A' states. Using the NACTs, the adiabatic-to-diabatic transformation (ADT) angle (γ_{12}) for 1 ^{2}A', 2 ^{2}A' states of CO_2^+ have been calculated. The ADT angle can be used to calculate diabatic potential energy surfaces from the adiabatic potential energy surfaces. Required number of states have been used to achieve quantization. NACTs have been calculated using the MOLPRO package at the state-averaged CASSCF level using the cc-pVTZ basis set.

In Chapter 2, the effect of hydration on cation-π interaction has been studied using Gaussian 09 suite of programs. The π–system under study is benzene (B) and the cations (M) studied are Na^+, K^+, Mg^{+2}, Ca^{+2} and Al^{+3}. Interaction energy values for the complexes MB_mW_n, $0 \leq n, m \leq 3$, $m + n \leq 3$ have been calculated at the MP2 level of theory using the 6-31G(d,p) basis set. Using these interaction energy values, the qualitative trend of relative affinity of different cations for benzene and water has been determined. The π–cloud thickness values have also been calculated for these system.

Chapter 1

Non-Adiabatic Interaction in CO_2^+

1.1 Introduction

Potential energy surfaces (PESs) calculated within the framework of Born-Oppenheimer approximation[1,2] (also called adiabatic potential energy surfaces) do not account for non-adiabatic effects (coupling between electronic and nuclear motion). In the Schrödinger equation for a molecular system, non-adiabatic effects appear in the form of non-adiabatic coupling terms (NACTs[1,2]). Without NACTs, no transition would be possible between the states.

Non-adiabatic interactions can be neglected when two PESs are far apart, but when they come close to each other then their magnitude becomes large. When two adiabatic PESs become degenerate then the point(s) of degeneracy is(are) called point(s) of conical/parabolical intersection(s) (CI/PI). Conical intersections of PESs are common in polyatomic molecules having three or more atoms. The CIs are formed between two adjacent adiabatic states. There is a rapid exchange of energy between the electronic and nuclear motion near the CIs and the Born-Oppenheimer approximation of the separability of electronic and nuclear motion breaks down. At these points of CI/PI, the NACTs become singular. When there is a degeneracy between states of the same symmetry, then such a point of degeneracy is called Jahn-Teller

conical intersection (JT-CI). If states of different symmetry intersect then these degeneracy points are called points of Renner-Teller (RT) intersection.

The inclusion of non-adiabatic effects and CIs is crucial for an accurate study of the dynamics. NACTs couple adiabatic PESs and are responsible for transition between the states. They play a key mechanistic role in the spectroscopy of polyatomic molecules, photochemistry and chemical kinetics. In several important cases such as dissociation, proton transfer and isomerization processes of polyatomic molecules or radiationless deactivation of the excited states, CIs provide an efficient channel for radiationless decay between electronic states. The CIs can provide an efficient channel for ultrafast interstate crossing in the femtosecond time scale.

Therefore, it is important to locate and characterize the CIs in molecular systems.

In this study, the NACTs and the adiabatic-to-diabatic transformation (ADT) angles for CO_2^+ system have been calculated. Using these ADT angles, diabatization can be carried out given the adiabatic PESs. This study is a part of the ongoing efforts in the lab to understand the dynamics of multiply charged polyatomic systems.

1.2 Beyond the Born-Oppenheimer Approximation

1.2.1 The Time-Independent Schrödinger Equation

The time-independent Schrödinger equation for a molecular system can be written as:

$$\hat{H}(R,r)\Psi(R,r) = E\Psi(R,r), \tag{1.1}$$

where $\hat{H}(R,r)$ and E are the total Hamiltonian and total energy of the molecular system, respectively. $\Psi(R,r)$ is the total wavefunction of the system, while R and r represent nuclear and electronic coordinates, respectively. The Hamiltonian consists

of following terms:

$$\hat{H}(R,r) = \hat{T}_N(R) + \hat{T}_e(r) + \hat{V}_{ee}(r) + \hat{V}_{eN}(R,r) + \hat{V}_{NN}(R), \tag{1.2}$$

where $\hat{T}_N$ and $\hat{T}_e$ are kinetic energy terms for nuclear and electronic part, respectively. The terms $\hat{V}_{ee}$, $\hat{V}_{eN}$ and $\hat{V}_{NN}$ represent potential energy for electronic-electronic repulsion, electronic-nuclear attraction and nuclear-nuclear repulsion, respectively.

Equation 1.2 can be written in a compact form as:

$$\hat{H}(R,r) = \hat{T}_N(R) + \hat{H}_e(r|R), \tag{1.3}$$

where $\hat{H}_e(r|R)$ represents the electronic Hamiltonian containing all other terms given in equation (1.2) except the nuclear kinetic energy term ($\hat{T}_N$). The use of symbol "|" in place of "," in $\hat{H}_e(r|R)$ indicates that it depends parametrically on 'R'.
The nuclear kinetic energy term ($\hat{T}_N$) has the following form:

$$\hat{T}_N(R) = -\frac{\hbar^2}{2\mu}\nabla^2(R), \tag{1.4}$$

where ∇ is the derivative with respect to nuclear coordinates R and μ is the corresponding mass term.

It is difficult to solve equation (1.1) in the given form for molecular systems and therefore we resort to an approximation called the *Born-Oppenheimer (BO) approximation.*

The Born-Oppenheimer approximation states that the slow motion of nuclei can be ignored while considering the fast electronic motion and nuclei can be assumed to be static. This approximation is justified on the account that the nuclei are much heavier when compared to the electrons. Therefore, we solve the Schrödinger equation for $\hat{H}_e$ part of the total Hamiltonian for a given R. Therefore, the electronic Schrödinger

equation within the framework of B-O approximation can be written as follows:

$$\hat{H}_e(r|R)|\zeta_j(r|R)\rangle = u_j(R)|\zeta_j(r|R)\rangle. \tag{1.5}$$

Equation (1.5) is essentially an eigenvalue problem. $\hat{H}_e$ contains nuclear-nuclear repulsion and nuclear-electronic attraction terms that depend parametrically on the nuclear coordinates. $|\zeta_j(r|R)\rangle$ is the eigenfunction corresponding to the j^{th}-eigenstate and $u_j(R)$ is the energy eigenvalue of the j^{th}-electronic eigenstate and is a function of nuclear coordinates.

The total wavefunction can be written as the Born-Oppenheimer expansion:[1,2]

$$|\Psi(R,r)\rangle = \sum_{j=1}^{\infty} \psi_j(R)|\zeta_j(r|R)\rangle, \tag{1.6}$$

where $\psi_j(R)$ is the nuclear wavefunction corresponding to the j^{th}–electronic state.

When $u_j(R)$, obtained from equation (1.5), is plotted against a range of R values then the surface (or curve in the case of a single nuclear coordinate), so obtained, is called the Potential Energy Surface (or Curve) (PES/PEC) calculated within the framework of Born-Oppenheimer approximation.

The PESs so obtained are called adiabatic potential energy surfaces. Interaction between the nuclear and electronic motion (also known as the non-adiabatic interaction) is completely ignored in the PESs thus obtained. These adiabatic PESs intersect in limited dimensions.

Substituting eq. (1.3) and eq. (1.6) in eq. (1.1), we obtain:

$$(\hat{T}_N(R) + \hat{H}_e(r|R)) \sum_{j=1}^{N} \psi_j(R)|\zeta_j(r|R)\rangle = E \sum_{j=1}^{N} \psi_j(R)|\zeta_j(r|R)\rangle \tag{1.7}$$

1.2.2 Breakdown of the B-O Approximation and Non-Adiabatic Effects:

Time Independent Adiabatic Schrödinger Equation

The adiabatic PESs calculated within the framework of Born-Oppenheimer approximation have an inherent limitation that they do not include non-adiabatic effects. The effect of nuclear motion can be ignored when the PECs are far apart and in such a situation non-adiabatic interactions are negligible between any two states. But when the PESs (of same symmetry) come close to each other then there is a rapid exchange of energy between the nuclear and electronic motion and the B-O approximation of separability of electronic and nuclear motion is no longer valid.

While dealing with an adiabatic PES, we deal only with the $\hat{H}_e$ part of the Hamiltonian and solve the Schrödinger equation for the electronic part only. To account for the non-adiabatic interaction, we solve the complete Schrödinger equation given in equation (1.7).

Equation (1.7) can be re-written as

$$\hat{T}_N(R)\sum_{j=1}^{N}\psi_j(R)|\zeta_j(r|R)\rangle + (\hat{H}_e(r|R) - E)\sum_{j=1}^{N}\psi_j(R)|\zeta_j(r|R)\rangle = 0. \tag{1.8}$$

As stated earlier, $\psi_j(R)$ depends on nuclear coordinates only, while $|\zeta_j(r|R)\rangle$ depends on both R and r. Keeping this fact in mind and using equations (1.4) and (1.5) and left multiplying equation (1.8) with $\langle\zeta_k(r|R)|$, we obtain:[3]

$$-\frac{\hbar^2}{2\mu}\nabla^2(R)\psi_k(R) + (u_k(R) - E)\psi_k(R) - \frac{\hbar^2}{2\mu}\sum_{j=1}^{N}(2\tau_{kj}.\nabla + \tau_{kj}^{(2)})\psi_j(R) = 0, \tag{1.9}$$

where k=1,....,N and τ_{kj} and $\tau_{kj}^{(2)}$ are the first and second-order NACTs, respectively.

Non-Adiabatic Coupling Terms

The first order NACTs have the following form:

$$\tau_{jk}(R) = \langle \zeta_j(r|R) | \nabla \zeta_k(r|R) \rangle. \tag{1.10}$$

From the form of the NACTs, it is evident that they connect two states. The first-order coupling terms form an anti-symmetric matrix, i.e.,

$$\tau_{jj}(R) = 0, \tag{1.11a}$$

$$\tau_{jk}(R) = -\tau_{kj}(R). \tag{1.11b}$$

And the second-order NACTs have the following form:

$$\tau^{(2)}_{jk}(R) = \langle \zeta_j(r|R) | \nabla^2 \zeta_k(r|R) \rangle, \tag{1.12}$$

where ∇^2 is the second derivative with respect to nuclear coordinates.

NACTs have a large magnitude in the vicinity of the CIs. At the points of CIs, the NACTs become singular. The NACTs and the topography of Born-Oppenheimer potential energy surfaces are related in the following manner given by the Hellmann-Feynman theorem:[4–7]

$$\tau_{jk} = \frac{\langle \zeta_j(r|R) | \nabla H_e | \zeta_k(r|R)}{u_k - u_j}.$$

Equation (1.10) can be written in a matrix form as follows:[8]

$$-\frac{\hbar^2}{2\mu}\nabla^2 \mathbf{\Psi} + (\boldsymbol{u} - E)\mathbf{\Psi} - \frac{\hbar^2}{2\mu}(2\boldsymbol{\tau}.\nabla + \boldsymbol{\tau}^{(2)})\mathbf{\Psi} = 0 \tag{1.13}$$

where $\mathbf{\Psi}$ represents the matrix that contains the nuclear functions $\{ \psi_j(R), j{=}1...N \}$ and $\boldsymbol{u}$ is a diagonal matrix that contains the eigenvalues of the electronic Schrödinger equation. $\boldsymbol{\tau}$ and $\boldsymbol{\tau}^{(2)}$ are matrices containing first and second order NACTs, respectively. The dot (.) represents the scalar product.

A detailed description of the B-O approximation and non-adiabatic effects requires a brief mathematical introduction. Therefore, the next section deals with some mathematical topics like Hilbert space, first order differential equation and its solutions and Curl-Divergence equations, etc. After getting acquainted with these mathematical aspects we shall return to the Born-Oppenheimer equation.

1.3 Mathematical Introduction

1.3.1 Hilbert Space

A complete basis set of eigenfunctions of electronic Schrödinger equation $\{\ |\zeta_j(r|R)\rangle, j = 1...N\ \}$ spans the Hilbert space.
They follow the *resolution of unity*:

$$\boldsymbol{I} = \sum_{k=1}^{N} |\zeta_k(r|R)\rangle\langle\zeta_k(r|R)|. \tag{1.14}$$

Any function $|\xi(r|R)\rangle$ can be expanded in terms of a linear combination of $|\zeta_k(r|R)\rangle$, with the coefficient of expansion being the overlap between the two functions:

$$|\xi(r|R)\rangle = \sum_{k=1}^{N} |\zeta_k(r|R)\rangle\langle\zeta_k(r|R)|\xi(r|R\rangle. \tag{1.15}$$

A complete Hilbert space is spanned by an infinite number of electronic eigenfunctions. But for numerical purposes, we cannot deal with a space having infinite basis. Therefore, we have to devise a *quasi-complete Hilbert space* involving a finite group of states, which gives nearly the same results as Hilbert space spanned by an infinite number of states. The space spanned by these finite group of states is called a *Hilbert subspace*.
In the case of a PES, we deal with the Hilbert space at a given nuclear configuration (R). But in the case of NACTs, we encounter the derivatives with respect to nuclear coordinates (R). That means that in the case of the NACTs, nearby Hilbert spaces have to be taken into account. Therefore, we define the relation between the points

of Hilbert space. The connection between points of Hilbert space is given by:[9]

$$|\zeta_k(r|R+\Delta R)\rangle = \sum_{j=1}^{N}(\delta_{kj} - \Delta R.\tau_{kj})|\zeta_j(r|R), \tag{1.16}$$

where δ_{kj} is the Kronecker delta function. The above expression holds for Hilbert subspace as well. The above equation suggests that NACTs connect a point R of Hilbert space with the points in its close proximity.

1.3.2 Curl Equation

The Curl equation for vector quantities is given as:

$$\boldsymbol{H} = \nabla \times \boldsymbol{\tau}, \tag{1.17}$$

where $\boldsymbol{H}$ and $\boldsymbol{\tau}$ are vector quantities. In this case, the z-component of $\boldsymbol{H}$ has the following form:

$$\boldsymbol{H}_z = \frac{\partial \tau_x}{\partial y} - \frac{\partial \tau_y}{\partial x}. \tag{1.18}$$

This is called the abelian-case. If we have a matrix in the place of a vector, then the Curl equation changes significantly and it assumes the following form in the case of a two coordinates (say p, q) system:

$$F_{pq} = \frac{\partial \tau_p}{\partial q} - \frac{\partial \tau_q}{\partial p} - [\tau_p, \tau_q]. \tag{1.19}$$

This situation is known as a *non-abelian case* and the above equation is known as an *extended* curl equation. Equation (1.19) can be written in a compact form as follows:

$$\boldsymbol{F} = \boldsymbol{H} - \boldsymbol{T}, \tag{1.20}$$

where

$$\boldsymbol{H}_{pq} = \frac{\partial \tau_p}{\partial q} - \frac{\partial \tau_q}{\partial p} \tag{1.21}$$

and

$$\boldsymbol{T}_{pq} = [\tau_p, \tau_q] = [\tau \times \tau]. \tag{1.22}$$

Using the *resolution of unity* (equation (1.14)) property of Hilbert space, it can be proven that for a Hilbert space, $\boldsymbol{F}$ has to be identically zero,[8,10] i.e.,

$$\boldsymbol{F} = 0. \tag{1.23}$$

1.3.3 Divergence Equation

In the Hilbert space, the **divergence** of the first-order non-adiabatic coupling terms ($\nabla\tau_{jk}$) can be written in the following form:

$$\nabla\tau_{jk} = \tau_{jk}^{(2)} - \sum_{i=1}^{N} \tau_{ji}\tau_{ik}, \tag{1.24}$$

which, in matrix form, can be written as:[8,10,11]

$$\nabla\boldsymbol{\tau} = \boldsymbol{\tau}^{(2)} - \boldsymbol{\tau}^2. \tag{1.25}$$

Equation (1.25) is called the *extended* divergence equation.

1.3.4 The First Order Differential Equation

We consider the following first order differential equation:

$$\nabla\boldsymbol{\Omega}(R) + \boldsymbol{\tau}(\boldsymbol{R})\boldsymbol{\Omega}(\boldsymbol{R}) = 0, \tag{1.26}$$

where $\boldsymbol{\Omega}(\boldsymbol{R})$ is a scalar matrix and $\boldsymbol{\tau}(\boldsymbol{R})$ is an anti-symmetric vector matrix. $\boldsymbol{R}$ is a point in configuration space.

Analyticity of a First Order Differential Equation

For equation (1.26) to have an ***analytic*** solution, the extended curl equation given in expression (1.19) has to be zero. From equation (1.23), we know that for an extended curl equation ($\boldsymbol{F}$) to be zero, the group of states involved must form the Hilbert space (or subspace).

Orthogonality

A consequence of the $\boldsymbol{\tau}$ matrix being anti-symmetric is that the scalar matrix $\boldsymbol{\Omega(R)}$ in equation (1.26) is orthogonal i.e.:

$$\boldsymbol{\Omega\Omega^{\dagger} = I = \Omega^{\dagger}\Omega}. \tag{1.27}$$

Solution of a First Order Differential Equation

In general, first order differential equations of the type

$$\nabla f(x) + t(x)f(x) = 0$$

have solutions in the following form:

$$f(x) = f_0(e^{-\int_{x_0}^{x} t(x').dx'}).$$

But in our case, we have matrices as variables. Therefore, the usual techniques for solving equation (1.26) cannot be employed. Here a different method known as propagation[12–14] is employed. Equation (1.26) is solved along a contour Γ, which starts from a point $\boldsymbol{R}_0$ and goes upto point $\boldsymbol{R}$ in configuration space. The scalar matrix has an initial value of $\boldsymbol{\Omega(R_0)}$.

Finally, upon solving the differential equation, we obtain:

$$\boldsymbol{\Omega(R|\Gamma)} = \wp exp\left\{-\int_{\boldsymbol{R_0}}^{\boldsymbol{R}} \boldsymbol{\tau(R'|\Gamma).dR'}\right\}\boldsymbol{\Omega(R_0)}. \tag{1.28}$$

Since matrix multiplication is not commutative, we put an ordering operator $\wp$ in the equation that ensures the multiplication in a definite order along the contour Γ. The dot (.) signifies the scalar product between the vectorial quantities $\boldsymbol{\tau(R'|\Gamma)}$ and $\boldsymbol{dR'}$ in the above equation which indicates that we deal with a *tangential* component of NACTs along the contour.

For a closed contour, equation (1.28) will look like:

$$\boldsymbol{\Omega(R_0|\Gamma)} = \wp exp\left\{-\oint_{\Gamma} \boldsymbol{\tau(R'|\Gamma).dR'}\right\}.\boldsymbol{\Omega(R_0)}. \tag{1.29}$$

A portion of equation (1.29) is defined as:

$$\boldsymbol{D(\Gamma)} = \wp exp\left\{-\oint_{\Gamma} \boldsymbol{\tau(R'|\Gamma).dR'}\right\}. \tag{1.30}$$

Equation (1.30) has a special significance and it will be discussed later.

1.4 Diabatization

1.4.1 Adiabatic Schrödinger Equation

After discussing the relevant mathematics, we shall now start with equation (1.13) :

$$-\frac{\hbar^2}{2\mu}\nabla^2\boldsymbol{\Psi} + (\boldsymbol{u} - E)\boldsymbol{\Psi} - \frac{\hbar^2}{2\mu}(2\boldsymbol{\tau}.\nabla + \boldsymbol{\tau}^{(2)})\boldsymbol{\Psi} = 0 \tag{1.13}$$

We can write the second-order NACTs ($\boldsymbol{\tau}^{(2)}$) in terms of the first-order NACTs ($\boldsymbol{\tau}$) using the divergence equation in Hilbert space as given in equation (1.25). Substituting equation (1.25) in equation (1.13), we obtain:

$$-\frac{\hbar^2}{2\mu}\nabla^2\boldsymbol{\Psi} + \left(\boldsymbol{u} - \frac{\hbar^2}{2\mu}\boldsymbol{\tau}^2 - E\right)\boldsymbol{\Psi} - \frac{\hbar^2}{2\mu}(2\boldsymbol{\tau}.\nabla + \nabla\tau)\boldsymbol{\Psi} = 0. \tag{1.31}$$

It can be shown that

$$(\nabla + \boldsymbol{\tau})^2\boldsymbol{\Psi} = (\nabla^2 + \boldsymbol{\tau}^2 + 2\boldsymbol{\tau}.\nabla + \nabla\boldsymbol{\tau})\boldsymbol{\Psi}. \tag{1.32}$$

Substituting equation (1.32) in equation (1.31), a more compact form[13,15] of equation (1.31) is obtained:

$$-\frac{\hbar^2}{2\mu}(\nabla + \boldsymbol{\tau})^2\boldsymbol{\Psi} + (\boldsymbol{u} - E)\boldsymbol{\Psi} = 0. \tag{1.33}$$

Equation (1.33) is a nuclear Schrödinger equation within the adiabatic framework in Hilbert space formed by a finite group of states. We cannot solve this equation because of the quantity $\boldsymbol{\tau}$ present in equation (1.33). In the region of configuration space, $\boldsymbol{\tau}$ (NACTs) may become singular (at CI/PI) leaving the whole equation unsolvable. Therefore, what we would like to do next is to eliminate $\boldsymbol{\tau}$ from equation (1.33).

1.4.2 Adiabatic-to-Diabatic Transformation Matrix and its Properties

For the purpose of eliminating τ from equation (1.33), we define a matrix which is called the adiabatic-to-diabatic transformation (ADT) matrix $\boldsymbol{A(R)}$ as follows:[8,11,15,16]

$$\boldsymbol{\Psi(R)} = \boldsymbol{A(R)}\boldsymbol{\chi(R)}. \tag{1.34}$$

$\boldsymbol{\chi(R)}$ can be chosen to satisfy the equation (1.34). It does not contain the NACTs.

Next, we assume that $\boldsymbol{A(R)}$ is a solution of the first order differential vector equation given in equation (1.26). Therefore, we can write:

$$\nabla\boldsymbol{A(R)} + \boldsymbol{\tau(R)}\boldsymbol{A(R)} = \boldsymbol{0}. \tag{1.35}$$

Some of the properties of $\boldsymbol{A(R)}$ emanate automatically from the fact that it is a solution to the first order differential vector equation.

- For equation (1.35) to have an analytical solution, the corresponding extended curl equation (given in equation 1.19) has to be zero. In section 1.3.4 it has been

discussed that the necessary and sufficient condition for this is that the states involved form a *Hilbert (sub)space*.

- $\boldsymbol{A(R)}$ is an orthogonal matrix as $\boldsymbol{\tau(R)}$ is an anti-symmetric matrix (section 1.3.4).

$$\boldsymbol{A}\boldsymbol{A}^{\dagger} = \boldsymbol{I} = \boldsymbol{A}^{\dagger}\boldsymbol{A}. \tag{1.36}$$

Now, substituting equation (1.34) in equation (1.33), we obtain:

$$-\frac{\hbar^2}{2\mu}(\nabla + \boldsymbol{\tau})^2\boldsymbol{A}(\boldsymbol{R})\boldsymbol{\chi}(\boldsymbol{R}) + (\boldsymbol{u}(\boldsymbol{R}) - E)\boldsymbol{A}(\boldsymbol{R})\boldsymbol{\chi}(\boldsymbol{R}) = 0. \tag{1.37}$$

Expanding the $(\nabla + \boldsymbol{\tau})^2\boldsymbol{A}(\boldsymbol{R})\boldsymbol{\chi}(\boldsymbol{R})$ part, we obtain:

$$(\nabla+\boldsymbol{\tau})^2\boldsymbol{A}\boldsymbol{\chi} = 2(\nabla\boldsymbol{A}).(\nabla\boldsymbol{\chi})+\boldsymbol{A}\nabla^2\boldsymbol{\chi}+(\nabla^2\boldsymbol{A})\boldsymbol{\chi}+(\nabla\boldsymbol{\tau})\boldsymbol{A}\boldsymbol{\chi}+2\boldsymbol{\tau}(\nabla\boldsymbol{A})\boldsymbol{\chi}+2\boldsymbol{\tau}\boldsymbol{A}(\nabla\boldsymbol{\chi})+\boldsymbol{\tau}^2\boldsymbol{A}\boldsymbol{\chi}. \tag{1.38}$$

which, upon rearrangement can be written as:

$$(\nabla + \boldsymbol{\tau})^2\boldsymbol{A}\boldsymbol{\chi} = \boldsymbol{A}\nabla^2\boldsymbol{\chi} + 2(\nabla\boldsymbol{A} + \boldsymbol{\tau}\boldsymbol{A}).\nabla\boldsymbol{\chi} + \{(\boldsymbol{\tau}) + \nabla).(\nabla\boldsymbol{A} + \boldsymbol{\tau}\boldsymbol{A})\}\boldsymbol{\chi}. \tag{1.39}$$

Using equation (1.35), equation (1.39) gets simplified to the following expression:

$$(\nabla + \boldsymbol{\tau})^2\boldsymbol{A}(\boldsymbol{R})\boldsymbol{\chi}(\boldsymbol{R}) = \boldsymbol{A}(\boldsymbol{R})\nabla^2\boldsymbol{\chi}(\boldsymbol{R}). \tag{1.40}$$

Now, substituting equation (1.40) in equation (1.37), we obtain:

$$-\frac{\hbar^2}{2\mu}\boldsymbol{A}(\boldsymbol{R})\nabla^2\boldsymbol{\chi}(\boldsymbol{R}) + (\boldsymbol{u}(\boldsymbol{R}) - E)\boldsymbol{A}(\boldsymbol{R})\boldsymbol{\chi}(\boldsymbol{R}) = 0. \tag{1.41}$$

By left multiplying this equation with $\boldsymbol{A}^{\dagger}(\boldsymbol{R})$, we obtain

$$-\frac{\hbar^2}{2\mu}\boldsymbol{A}^{\dagger}(\boldsymbol{R})\boldsymbol{A}(\boldsymbol{R})\nabla^2\boldsymbol{\chi}(\boldsymbol{R}) + \boldsymbol{A}^{\dagger}(\boldsymbol{R})(\boldsymbol{u}(\boldsymbol{R}) - E)\boldsymbol{A}(\boldsymbol{R})\boldsymbol{\chi}(\boldsymbol{R}) = 0. \tag{1.42}$$

Equation (1.42) can be re-arranged to the following form:

$$-\frac{\hbar^2}{2\mu}\boldsymbol{A}^{\dagger}(\boldsymbol{R})\boldsymbol{A}(\boldsymbol{R})\nabla^2\boldsymbol{\chi}(\boldsymbol{R}) + \{(\boldsymbol{A}^{\dagger}(\boldsymbol{R})\boldsymbol{u}(\boldsymbol{R})\boldsymbol{A}(\boldsymbol{R})) - E(\boldsymbol{A}^{\dagger}(\boldsymbol{R})\boldsymbol{A}(\boldsymbol{R}))\}\boldsymbol{\chi}(\boldsymbol{R}) = 0. \tag{1.43}$$

Substituting equation (1.36), equation (1.43) reduces to the following form:

$$-\frac{\hbar^2}{2\mu}\nabla^2\boldsymbol{\chi}(\boldsymbol{R}) + (\boldsymbol{W}(\boldsymbol{R}) - E)\boldsymbol{\chi}(\boldsymbol{R}) = 0, \tag{1.44}$$

where $\boldsymbol{W(R)}$ is a diabatic potential matrix and has the following form:

$$\boldsymbol{W}(\boldsymbol{R}) = \boldsymbol{A}^{\dagger}(\boldsymbol{R})\boldsymbol{u}(\boldsymbol{R})\boldsymbol{A}(\boldsymbol{R}). \tag{1.45}$$

Therefore, if we have the ADT matrix $\boldsymbol{A}(\boldsymbol{R})$ and the diagonal adiabatic potential matrix $\boldsymbol{u}(\boldsymbol{R})$, then we can have the diabatic potential matrix as per the scheme given in equation (1.45). The matrix $\boldsymbol{u}(\boldsymbol{R})$ can be obtained from the electronic Schrödinger equation (see equation 1.5). From equation (1.45), it is clear that adiabatic potential matrix ($\boldsymbol{u}$) is an eigenvalue matrix for the diabatic potential matrix $\mathbf{W}$. Till now, we do not know how to obtain the ADT matrix $\boldsymbol{A}(\boldsymbol{R})$.

To obtain the ADT matrix $\boldsymbol{A}(\boldsymbol{R})$, we solve the first order differential vector equation given in equation (1.35). It is solved as per method given in section 1.3.4. Equation (1.35) is solved along a suitably chosen contour Γ to include the configuration space of interest.

So the solution for equation (1.35) along a contour Γ having initial point $\boldsymbol{R_0}$ will resemble equation (1.28):[12]

$$\boldsymbol{A}(\boldsymbol{R}|\boldsymbol{\Gamma}) = \wp exp\left\{-\int_{\boldsymbol{R_0}}^{\boldsymbol{R}} \boldsymbol{\tau}(\boldsymbol{R'}|\Gamma).\boldsymbol{dR'}\right\}\boldsymbol{A}(\boldsymbol{R_0}). \tag{1.46}$$

The dot (.) signifies the scalar product between $\boldsymbol{\tau(R'|\Gamma)}$ and $\boldsymbol{dR'}$, which implies that we deal with the tangential components of NACTs along the given contour Γ.

For the sake of convenience and simplifying the numerical procedure, we often choose

the contour to be circular. When we have a circular contour, the variables are (q, φ), q being the radius of the contour and φ is the angle subtended at the centre from a suitably chosen reference.
Equation (1.46) assumes the following form for a circular contour:

$$\boldsymbol{A}(\varphi|q) = \wp exp\left\{-\int_0^{\varphi} \boldsymbol{\tau}(q,\varphi'|\Gamma)d\varphi'\right\}\boldsymbol{A_0}(q). \tag{1.47}$$

In the equation above, we have taken only the angular part in the integration as it constitutes the tangential component of NACTs along the given contour and the scalar product has been dropped for the same reason. $\boldsymbol{A_0}(q)$ in equation (1.47) is the initial value of the matrix $\boldsymbol{A}(q)$ at $\varphi = 0$.

At the end-of-the-contour integration, the upper limit of integration becomes $\varphi = 2\pi$ and equation (1.47) becomes:

$$\boldsymbol{A}(\varphi|q) = \wp exp\left\{-\int_0^{2\pi} \boldsymbol{\tau}(q,\varphi'|\Gamma)d\varphi'\right\}\boldsymbol{A_0}(q). \tag{1.48}$$

We define a quantity $\boldsymbol{D}(q)$ as:[10,17–19]

$$\boldsymbol{D}(q) = \wp exp\left\{-\int_0^{2\pi} \boldsymbol{\tau}(q,\varphi'|\Gamma)d\varphi'\right\} \tag{1.49}$$

Therefore, to calculate the ADT matrix, we choose a suitable circular contour, which includes the region of interest and calculate angular NACTs for it. These angular NACTs, in our case, have been calculated numerically using the MOLPRO software package.[20] In the next section, the use of these angular NACTs for calculating the ADT matrix is discussed.

The diabatic potential matrix $\boldsymbol{W}$ obtained using equation (1.45) may become multivalued if it surrounds one or more CIs. The Schrödinger equation in equation (1.44) cannot be solved unless $\boldsymbol{W}$ are single valued. It can be proved that **for a diabatic potential matrix *W(R)* to be single valued in a region of configuration space, $\boldsymbol{D}(\Gamma)$ has to be diagonal with phase factors.**[17,18]

1.5 Methodology

1.5.1 A 2-State System

In the case of a 2-state system, the non-adiabatic coupling matrix (NACM) will be a 2×2 anti-symmetric matrix. Therefore, for the case involving only two states 1 and 2, the NACM has the following form:

$$\boldsymbol{\tau}(q,\varphi) = \begin{pmatrix} 0 & \tau_{12} \\ -\tau_{12} & 0 \end{pmatrix}. \tag{1.50}$$

The simplest 2×2 real orthogonal ADT matrix $\boldsymbol{A}(q,\varphi)$ that we can think of is the following:

$$\boldsymbol{A}(q,\varphi) = \begin{pmatrix} cos\gamma_{12}(q,\varphi) & sin\gamma_{12}(q,\varphi) \\ -sin\gamma_{12}(q,\varphi) & cos\gamma_{12}(q,\varphi) \end{pmatrix}, \tag{1.51}$$

where γ_{12}(q,φ) is the angle to be determined.

The ADT matrix $\boldsymbol{A}(q,\varphi)$ has to be a solution of the first order differential vector equation given in equation (1.35). We determine γ from the condition that the matrix $\boldsymbol{A}(q,\varphi)$ satisfies the first order differential equation. If we substitute equation (1.50) and equation (1.51) in equation (1.35), then we get an expression for $\gamma(q,\varphi)$ as given below:

$$\nabla\gamma_{12}(q,\varphi) + \tau_{12}(q,\varphi) = 0 \tag{1.52}$$

Equation (1.52) is also a first order differential equation and is solved in the same fashion as given in the section 1.3.4. The equation (1.52) has to be solved along a suitably chosen circular contour Γ. The solution of equation (1.52) along the contour Γ is given below:

$$\gamma_{12}(\varphi|q) = \int_0^{\varphi} \tau_{12}(q,\varphi)d\varphi. \tag{1.53}$$

As it was stated earlier, the angular component is tangential to the contour. Therefore, we are not required to take the scalar product. γ is called the *adiabatic-to-diabatic*

transformation angle.

At the end-of-the-contour integration, the upper limit of integration is $\varphi = 2\pi$ and the angle so obtained is called the *topological phase*. In this case, equation (1.53) has the following form:

$$\gamma(0, 2\pi|q, \Gamma) = \alpha_{12}(q) = \int_0^{2\pi} \tau_{12}(q, \varphi) d\varphi. \tag{1.54}$$

When we substitute the topological phase ($\alpha_{12}(q)$) in place of the ADT angle ($\gamma_{12}(\varphi)|q$) in the matrix given in equation (1.50), we get the *topological matrix* $\boldsymbol{D}(\Gamma)$:

$$\boldsymbol{D(\Gamma)} = \begin{pmatrix} cos\alpha_{12}(q) & sin\alpha_{12}(q) \\ -sin\alpha_{12}(q) & cos\alpha_{12}(q) \end{pmatrix} \tag{1.55}$$

As it was stated earlier, we obtain a single valued diabatic potential energy matrix only when $\boldsymbol{D(\Gamma)}$ is diagonal. From equation (1.55), it is clear that for $\boldsymbol{D(\Gamma)}$ to be diagonal, the topological phase ($\alpha_{12}(q)$) has to be an integer multiple of π:

$$\alpha_{12}(q, \varphi) = \int_0^{2\pi} \tau_{12}(q, \varphi) d\varphi = n\pi, \tag{1.56}$$

where $n \in \mathbb{Z}$. This is called the *quantization condition*. Therefore, we integrate the angular NACTs obtained for a suitably chosen circular contour including the configuration space of interest over the range [0,2π] to get the quantization condition. Once the quantization condition is fulfilled, the adiabatic potential energy surfaces can be diabatized in the configuration space surrounded by the contour.
In this case, the diabatic potential matrix $\boldsymbol{W(R)}$ is a 2 $\times$ 2 matrix given below:

$$\boldsymbol{W(R)} = \begin{pmatrix} W_{11}(R) & W_{12}(R) \\ W_{21}(R) & W_{22}(R) \end{pmatrix} \tag{1.57}$$

Since we have the ADT matrix $\boldsymbol{A}$ in terms of coordinates (q, φ), we have to transform the coordinates from (q, φ) to the coordinate system of adiabatic potential matrix $\boldsymbol{u}$. Once this coordinate transformation of the $\boldsymbol{A}$ matrix is done (say coordinate

$\boldsymbol{R}$), diabatization is carried out as per scheme given in equation (1.45) which has been written below again:

$$\boldsymbol{W}(\boldsymbol{R}) = \boldsymbol{A}^{\dagger}(\boldsymbol{R})\boldsymbol{u}(\boldsymbol{R})\boldsymbol{A}(\boldsymbol{R}) \tag{1.40}$$

After the matrix multiplication, we get a 2 × 2 diabatic potential matrix similar to the one in equation (1.57) and the corresponding matrix elements are given below:

$$W_{11}(R) = u_1 cos^2\gamma(R) + u_2 sin^2\gamma(R) \tag{1.58a}$$

$$W_{22}(R) = u_1 sin^2\gamma(R) + u_2 cos^2\gamma(R) \tag{1.58b}$$

$$W_{12}(R) = (u_1 - u_2) cos\gamma(R) sin\gamma(R) \tag{1.58c}$$

1.5.2 A 3-State System

Theoretically, we have to include NACTs between all states (infinite) to get an *exact* quantization condition. But, because of practical consideration, we select those electronic states among which the non-adiabatic effects are significant (which are the states spanning the Hilbert subspace) and lead us to quantization condition to a *reasonable* extent. When only two adjacent states are nearing each other then the Hilbert space spanned by these two states is *sufficient* enough to lead us to a reasonable quantization condition. Such a case is discussed in section 1.5.1.

Sometimes, the quantization condition is not fulfilled using only two states because of interference from (an)other nearby state(s). Non-adiabatic effects from these states are also significant and have to be included to get the quantization condition.[21,22] As a first step to achieve quantization, we include a third state in our calculations and the non-adiabatic coupling matrix (NACM) gets modified. The resulting 3 × 3 anti-symmetric matrix is given in the equation below:

$$\boldsymbol{\tau}(q,\varphi) = \begin{pmatrix} 0 & \tau_{12} & \tau_{13} \\ -\tau_{12} & 0 & \tau_{23} \\ -\tau_{13} & -\tau_{23} & 0 \end{pmatrix}. \tag{1.59}$$

The three-state adiabatic-to-diabatic transformation (ADT) matrix ($\boldsymbol{A}^{(3)}$) has to be a 3 × 3 orthogonal matrix . It can be obtained through the product of three rotation matrices, namely $\boldsymbol{Q}_{12}^{(3)}(\gamma_{12})$, $\boldsymbol{Q}_{13}^{(3)}(\gamma_{13})$, and $\boldsymbol{Q}_{23}^{(3)}(\gamma_{23})$ where γ_{12}, γ_{13} and γ_{23} are Euler rotation angles.[23–28]

Therefore, the ADT matrix ($\boldsymbol{A}^{(3)}$) will have the following form:

$$\boldsymbol{A}^{(3)} = \boldsymbol{Q}_{\boldsymbol{12}}^{(\boldsymbol{3})}(\boldsymbol{\gamma_{12}})\boldsymbol{Q}_{\boldsymbol{23}}^{(\boldsymbol{3})}(\boldsymbol{\gamma_{23}})\boldsymbol{Q}_{\boldsymbol{13}}^{(\boldsymbol{3})}(\boldsymbol{\gamma_{13}}). \tag{1.60}$$

The orthogonal $\boldsymbol{Q}_{12}^{(3)}(\gamma_{12})$ matrix can be written in the following form:

$$\boldsymbol{Q}_{\boldsymbol{12}}^{(\boldsymbol{3})}(\boldsymbol{\gamma_{12}}) = \begin{pmatrix} cos\gamma_{12}(q,\varphi) & sin\gamma_{12}(q,\varphi) & 0 \\ -sin\gamma_{12}(q,\varphi) & cos\gamma_{12}(q,\varphi) & 0 \\ 0 & 0 & 1 \end{pmatrix}. \tag{1.61}$$

Other matrices $\boldsymbol{Q}_{13}^{(3)}(\gamma_{13})$ and $\boldsymbol{Q}_{23}^{(3)}(\gamma_{23})$ can be written in a similar manner and are orthogonal.

The ADT matrix ($\boldsymbol{A}^{(3)}$) thus obtained using equation (1.60) will be an orthogonal matrix as it is a product of three orthogonal matrices [$\boldsymbol{Q}_{12}^{(3)}(\gamma_{12})$, $\boldsymbol{Q}_{13}^{(3)}(\gamma_{13})$, $\boldsymbol{Q}_{23}^{(3)}(\gamma_{23})$]. It has the following form:

$$\boldsymbol{A}^{(\boldsymbol{3})}(\boldsymbol{\Gamma}) = \begin{pmatrix} c_{12}c_{13} - s_{12}s_{13}s_{23} & s_{12}s_{23} & c_{12}s_{13} + c_{12}s_{23}c_{13} \\ -s_{12}c_{13} - c_{12}s_{23}s_{13} & c_{12}c_{23} & -s_{12}s_{13} + c_{12}s_{23}c_{13} \\ -c_{23}s_{13} & -s_{23} & c_{23}c_{13} \end{pmatrix} \tag{1.62}$$

Here c_{jk} is $\cos(\gamma_{jk})$ and s_{jk} is $\sin(\gamma_{jk})$. γ_{jk} are corresponding ADT angles.

If $\gamma_{jk}(\varphi|\Gamma)$ is replaced by the corresponding end-of-the-contour integrated ADT angle $\gamma_{jk}(0, 2\pi|\Gamma)$, which is denoted as $\alpha(\Gamma)$, then we get the corresponding topological matrix $\boldsymbol{D}^{(3)}(\boldsymbol{\Gamma})$.

We have ensured the orthogonality of matrix $\boldsymbol{A}^{(3)}$, but at the same time it has to be

a solution of the first order differential equation given in equation (1.35). Substituting

$$\boldsymbol{A}^{(3)} = \boldsymbol{Q}^{(3)}_{12}(\gamma_{12})\boldsymbol{Q}^{(3)}_{13}(\gamma_{13})\boldsymbol{Q}^{(3)}_{23}(\gamma_{23})$$

(order is important) in equation (1.35), we get a set of coupled linear differential equations corresponding to three ADT angles as follows:

$$\nabla\gamma_{12} = -\tau_{12} - tan\gamma_{13}(\tau_{23}cos\gamma_{12} + \tau_{13}sin\gamma_{12}) \tag{1.63a}$$

$$\nabla\gamma_{13} = \tau_{23}sin\gamma_{12} - \tau_{13}cos\gamma_{12} \tag{1.63b}$$

$$\nabla\gamma_{23} = -(cos\gamma_{23})^{-1}(-\tau_{13}cos\gamma_{12} + \tau_{23}cos\gamma_{12}) \tag{1.63c}$$

The grad operator ∇ represents the derivative with respect to φ ($\partial/\partial\varphi$).
These linear coupled equations are solved to obtain the corresponding ADT angles.

To have a single valued diabatic potential matrix $\boldsymbol{W}$, the topological matrix $\boldsymbol{D}^{(3)}(\Gamma)$ has to be diagonal. For the topological matrix $\boldsymbol{D}^{(3)}(\Gamma)$ to be diagonal, corresponding topological phases must be quantized. Since we are considering the 1 ^{2}A' and 2 ^{2}A' states of CO_2^+, so we focus on quantization of $\alpha_{12}(q)$.

1.5.3 Signflips of Electronic Eigenfunctions

Longuet-Higgins found that when electronic eigenfunctions surround a point of degeneracy they acquire a phase, which causes flip of sign of these eigenfunctions.[29–31] This fact has a special significance in relation to confirm the existence of a CI in a given configuration space.
The topological matrix $\boldsymbol{D}(\Gamma)$ matrix also satisfies the following relation:

$$|\boldsymbol{\zeta}(r|R_0|R_0)\rangle = \boldsymbol{D}(\Gamma)|\boldsymbol{\zeta}(r|R_0)\rangle, \tag{1.64}$$

where $|\boldsymbol{\zeta}(r|R_0)\rangle$ is the (column) matrix containing the electronic eigenfunctions at the initial point R_0 of the closed contour Γ. $\boldsymbol{\zeta}(r|R_0|R_0)\rangle$ is the (column) matrix containing the electronic eigenfunctions after they transported along the closed contour Γ.
Equation 1.64 suggest that the electronic eigenfunctions corresponding to the states

having a degeneracy point in the region of the configuration space surrounded by a closed contour flip their signs when transported along the closed contour.

In a two states system, the corresponding electronic eigenfunctions are (say) $|\zeta_1(r|R)\rangle$, $|\zeta_2(r|R)\rangle$. If these states have a degeneracy point (CI) in the configuration space enclosed by a close contour Γ then the matrix $\boldsymbol{D}(\Gamma)$ (given in equation (1.55)) will be a 2×2 matrix having -1 on the diagonal and 0 on off-diagonal positions. For this to happen, the topological phase α have to be an odd-integer multiple of π. When the closed contour encloses one CI then the odd-integer is 1. Therefore, we get the end-of-the-contour value of the ADT angle (topological phase) to be $\pm\pi$. Thus, $\boldsymbol{D}(\Gamma)$ results in a change in the sign when electronic eigenfunctions are transported along the contour Γ.

If the same states have two degeneracy points in the region surrounded by the closed contour then the electronic eigenfunctions flip their signs twice thus returning to their original form. Therefore, the $\boldsymbol{D}(\Gamma)$ matrix will have 1 on the diagonal and 0 on the off-diagonal positions. For this to happen, the end-of-the-contour ADT angle α has to be an even-integer multiple of π. When the closed contour Γ surrounds two CIs then the integer come out to be 0 or 2. Therefore, the value of the topological phase α obtained is $\pm 2\pi$.

Conversely, we can state that if we get the end-of-the-contour ADT angle to be π then the contour surround one CIs. Also, if it comes out to be 2π then the contour surrounds two CIs.

1.6 Numerical Considerations

1.6.1 Computational Details

CO_2^+ has 21 electrons, of which 15 are valence electrons and 6 are core electrons. It has 12 valence orbitals and 3 core orbitals. The ground state for CO_2^+ is $^2\Pi_g$. For the purpose of calculation, the symmetry has been taken to be C_s. Therefore, the states are of A' and A" symmetry.

To calculate the NACTs, the Molpro program package[20] has been used and the calculations have been carried out at the state-averaged complete active space self-consistent field (CASSCF) level of theory. The eleven valence electrons were distributed in the ten active orbitals, while the 5 orbitals (3 core orbitals + 2 valence orbitals) were kept closed. The Dunning's basis set[32] cc-pVTZ was used throughout the calculations. State-averaged three state calculations having equal weights have been carried out.

A numerical differentiation method (in Molpro) has been employed to calculate NACTs. In this method, electronic wavefunction for the states is calculated numerically at a given nuclear coordinate R. The wavefunction is also calculated in the vicinity (very small distance $\pm\Delta R$) of the given nuclear coordinate. Then a numerical differentiation is carried out. An average value (of (R, R-ΔR), (R, R + ΔR)) is taken. In this study, ΔR (in this case $\Delta\varphi$) is chosen to be 1.0 degree.

JT-NACTs (NACTs between states of the same symmetry) for 1 ^{2}A', 2 ^{2}A' and 3 ^{2}A' have been calculated. NACTs between (1,2) A', (2,3) A' and (1,3)A' are designated as τ_{12}, τ_{23} and τ_{13}, respectively. The ground state $^2\Pi_g$ for CO_2^+ is doubly degenerate and in C_s symmetry it splits into two states of different symmetry: 1 ^{2}A' and 1 ^{2}A". RT-NACTs between these two states have been calculated. Also the PECs for these 4 states (3 of ^{2}A' and 1 of ^{2}A") have been generated for different radii at the MCSCF level of theory using the cc-pVTZ basis set.

1.6.2 Numerical Aspects

In the present study, contours surrounding the region of configuration space of interest are chosen to be circular in the triatomic plane. Reasons for this circular plane are that it is numerically convenient to carry out calculations in a circular plane and the dynamics of the molecule is carried out in the triatomic plane.

For calculations, two schemes have been employed:

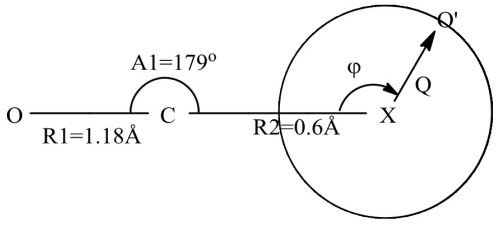

Figure 1.1: Coordinates used in the calculation of NACTs for Scheme 1

Scheme 1

The first scheme is shown in Figure 1.1 and is as follows – one C-O bond distance (R1=$r_{C\text{-}O}$) is kept fixed at 1.18 Å (R1 in Figure 1.1) and the other O (designated as O') revolves around a center (depicted as X in Figure 1.1) which is fixed at 0.6 Å from the C atom (R2) and the angle X – C – O (designated as **A1** in Figure 1.1) is fixed at 179°. The revolving radius (Q) is suitably chosen to encircle the configuration space of interest. The O' atom revolves in the range $\varphi = [0,2\pi]$ to complete the circular contour. The revolving O' atom has the closest distance to the C atom when $\varphi = 0$ and is farthest from C when $\varphi = \pi$.

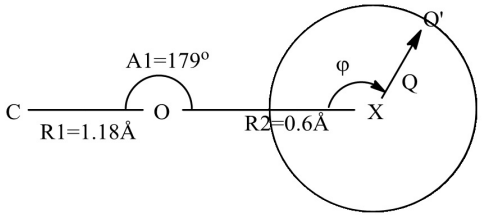

Figure 1.2: Coordinates used in the calculation of NACTs for Scheme 2

Scheme 2

The second scheme is shown in Figure 1.2 and is as follows: one C–O bond distance is fixed at 1.18 Å (designated as R1 in Figure 1.2) and the other O (designated as O') revolves around a center (depicted as X in Figure 1.2) which is fixed at 0.6 Å from the O atom (R2). The angle C – O – X (designated as **A1** in Figure 1.2) is fixed at 179^o . The revolving radius (Q) is suitably chosen to encircle the configuration space of interest. The O' atom revolves in the range $\varphi = [0,2\pi]$ to complete the circular contour. The revolving O' atom has the closest distance to the O atom when $\varphi = 0$ and is farthest from O when $\varphi = \pi$.

As stated earlier, the tangential component of NACTs along the contour is required to determine the ADT matrix. Since we have chosen a circular contour, the angular component forms the tangential part. Therefore, **the angle (φ) is varied to calculate the NACTs while keeping the radius (Q) fixed**. The Q values were varied to choose contours enclosing different areas.

1.7 Results and Discussion

1.7.1 Calculations of NACTs

As stated earlier, couplings between two states are negligible when they are far apart. But when they approach each other, the NACTs become significant. NACTs become singular at the point of degeneracy between two PECs. So while tracing a circular contour, when we go near a CI/PI, the NACTs become large and they decrease as we move away from the CI/PI. When NACTs are plotted as a function of φ, they show a spiky behaviour near the points of CIs. This behaviour can be observed in Figures 1.3[a-f] and 1.4[a-d].

While drawing plots of NACTs as a function of φ, the plots have been kept symmetric or anti-symmetric and continuous by flipping the sign of NACTs.

NACTs: Scheme 1

In the present study, as described in section 1.6.2 (scheme 1), one of the C-O distances was fixed at 1.18 Å while the other revolves with a fixed radius Q around a center located 0.6 Å from the C atom. The values of Q chosen in the study are Q = 0.2, 0.3, 1.0, 1.2, 1.4, 2.1, 2.2, 2.3 and 2.4 Å.

When Q = 0.2 and 0.3 Å, two states (1 A' and 2 A') yield quantization conditions adequately. That means that the third state does not interfere and as a consequence the values of the (1,3) NACTs are small. Plots for the NACTs vs φ are simple in these two cases. There are two simple spikes in the plots. These spiky NACTs and the (fulfilled) quantization condition (α_{12} close to π) show that there is one JT CI between 1 A' and 2 A' states in the region. Plots for NACTs vs φ are given in Figure 1.3[a-b].

When Q = 1.0, 1.2 and 1.4 Å, the revolving O' atom comes between C and O for $\varphi = 0$ resulting in a C–O'–O configuration. In these cases, the NACTs become complicated. 2-states (1, 2) NACTs are not adequate to give a correct quantization. (1, 3) NACTs become significantly larger. (1, 3) NACTs were taken into account to achieve quantization. It is because of the fact that large radii encircles the regions where the 3 A' state comes near the first two states. Plots for NACTs vs φ are given in Figure 1.3[c-e].

When Q = 2.1, 2.2, 2.3 and 2.4 Å, the O' atom goes past the O atom, thus making the configuration O' – O – C for $\varphi = 0$. Quantization is not achieved by the two lower states and a 3 - state calculation had to be carried to achieve quantization. Plots of NACTs vs φ are given in Figures 1.3[f] and 1.4[a-c].

NACTs: Scheme 2

NACTs were calculated for scheme 2 to ascertain the location of another CI (the first being ∼0.6 Å close to C in the direction away from O). The scheme has been described in section 1.6.2 and Figure 1.2. Values of Q chosen in this study are 0.4 and 1.2 Å. NACTs for Q = 0.4 Å are relatively simpler, while for Q = 1.2 Å they are a bit complicated. Three-state calculations are required in both cases to get quantization. Plots of NACTs vs φ are given in Figure 1.4[d-e]

1.7.2 Calculations of the (1,2) ADT angle

The ADT angle γ_{12}(q) for two states is calculated as per scheme given in equation (1.53), while an end-of-the-contour integration yields a topological phase (α_{12} (q,Γ)) as given in equation (1.54). A three-state calculation for the ADT angle is carried out by simultaneously solving coupled linear differential equations given in equations (1.63a) and (1.63b). These equations were solved using the software package Mathematica. End-of-the-contour integration of this three-state α_{12} (q,Γ) thus calculated gives the three-state topological phase.

ADT Angle: Scheme 1

For Q = 0.2 and 0.3 Å, the value of the topological phase for a 2-state calculation is 3.19 and 3.11, respectively. Therefore, for these smaller radii, the quantization is achieved by considering two states only. It can be concluded safely that the 3^{rd} state does not interfere for these small radii and correspondingly (1,3) NACTs are also small. When a 3-state calculation is carried out, it retains its quantization and the three-state topological phase comes out to be 3.05 and 3.11, respectively. Plots of 2-state and 3-state ADT angles (γ_{12}) vs φ are given in Figure 1.5[a-b].

For Q = 1.0, 1.2 and 1.4 Å where O' is going to the other side of C, the 2-state

topological phase does not fulfil the quantization condition adequately. Therefore, we may not get single valued diabatic potentials upon diabatization and the topological matrix ($\boldsymbol{D}$) is not diagonal. For this reason, three-state calculations as per equations (1.63a) and (1.63b) to get the ADT angle were carried out. These yield sufficiently quantized topological phases. Plots of the two and three state ADT angle (γ_{12}) against the angle (φ) are given in Figure 1.5[c-e]. For Q = 1.0, 1.2 and 1.4 Å, the two-state topological phase is 1.23, 2.55 and 1.83, respectively. The three-state topological phase for Q = 1.0, 1.2 and 1.4 are 3.24, 3.24 and 3.22, respectively.

For Q = 2.1, 2.2, 2.3 and 2.4 Å, where O' goes beyond O, the two-state topological phases are not quantized. Therefore, we add the 3^{rd} state into the calculation, which yields topological phases close to 2π for all cases except Q = 2.1. For Q = 2.1, the 3-state α_{12} is close to π. For Q = 2.1, 2-state and 3-state topological phases are 0.65 and 3.06, respectively. For Q = 2.2, 2.3 and 2.4, the 2-state topological phases are 1.84, 2.30 and 2.49, respectively, while the same for 3-state are 6.77, 6.35 and 6.16. Plots of the two and three state ADT angle (γ_{12}) against the angle (φ) are given in Figures 1.5[f] and 1.6[a-c].

Results given above indicate that up to Q $\leq$ 2.1Å the circular contours surround only one conical intersection, as results of 2-state and 3-state topological phases converge to π. For Q > 2.2Å, the 3-state topological phases converge to 2π, which implies that the contours surround two conical intersections. Since NACTs are spiky in the vicinity of $\varphi = 0$, another CI lies in the interval Q = [2.1-2.2].

All the results for 2 and 3 state α_{12} for scheme 1 are summarized and listed in Table 1.1.

Table 1.1: 2 and 3-state topological phase for 1 ^{2}A' and 2 ^{2}A' states for different Q values (scheme 1)

Q (Å)	**2-state α_{12} (in radian)**	**3-state α_{12} (in radian)**
0.2	3.19	3.05
0.3	3.11	3.06
1.0	1.23	3.24
1.2	2.55	3.24
1.4	1.83	3.24
2.1	0.65	3.22
2.2	1.84	6.77
2.3	2.30	6.35
2.4	2.49	6.16

ADT Angle: Scheme 2

As mentioned earlier, from the results of scheme 1, it is clear that there is a CI in the interval Q = [2.1-2.2] Å. To ascertain and locate the CI, scheme 2 was devised. Details are given in section 1.6.2 and Figure 1.2.

2-state and 3-state ADT angles for Q = 0.4 and 1.2 Å are calculated. The 2-state topological phase for Q = 0.4 comes out to be 3.47, which is close to π. 2-state and 3-state topological phase for Q = 1.2 Å are 2.51 and 3.10, respectively. Plots of 2-state and 3-state ADT angles (γ_{12}) vs φ are given in Figure 1.6[d-e]. All the results for 2 and 3 state α_{12} for scheme 2 are summarized and listed in Table 1.2.

Table 1.2: 2 and 3-state topological phase for 1 ^{2}A' and 2 ^{2}A' states for different Q values (scheme 2)

Q (Å)	**2-state α_{12} (in radian)**	**3-state α_{12} (in radian)**
0.4	3.47	NA
1.2	1.83	3.10

1.7.3 Potential Energy Curves

For the sake of completeness, potential energy curves for CO_2^+ have been drawn for 1 ^{2}A', 2 ^{2}A', 3 ^{2}A' and 1 ^{2}A" states for several Q values. PECs have been generated at the MCSCF level of theory using the cc-pVTZ basis set. The values of Q for which the PECs are drawn are 0.2, 0.3, 1.2, 2.1, 2.3 and 2.4 Å. Plots of the energy (hartree) against the revolving angle (φ) are given in Figure 1.7[a-f]. Potential energy of the system varies by ∼10-20 hartree when φ is varied in the range [0,2π]. Potential energy is maximum for $\varphi = 0$ because for this angle O' is closest to C and O atoms.

It can be inferred from Figure 1.7(a-c) that the PECs for Q = 0.2 and 0.3 Å show one CI between 1A' and 2A' states around $\varphi = \sim \frac{\pi}{6}$. In Figure 1.7(b), to make (1,2) A' CI visible for Q = 0.2, the potential energy curve is drawn for a relatively small range of angles *viz.* [-$\frac{\pi}{3}$,$\frac{\pi}{3}$]. 2 A' and 3 A' states also come close to each other around $\varphi = \sim \frac{\pi}{3}$. As we increase the value of Q, the PECs become more and more spikier because of large variation in the potential energy values. From figures 1.7[d-f], two CIs between 1 A' and 2 A' and 2 A' and 3 A' states can be observed. The 1 A" state is nearly degenerate with 1 A' for all values of φ except at some points.

1.8 Summary and Conclusion

NACTs and ADT angle for CO_2^+ were calculated and the results are summarized below. From the results of topological phase (α) values, we conclude that:

1. In scheme 1, quantization is adequately achieved with a two-state calculation for Q = 0.2, 0.3 Å. A three-state calculation for the same set of radii also yields the quantization condition.

2. For Q = 1.0, 1.2, 1.4, 2.1, 2.2, 2.3 and 2.4 Å, in scheme 1, a reasonable quantization condition is not achieved with the two state calculation. Therefore, we include a third state (3 ^{2}A'), in the calculation and this three-state calculation yields quantization condition adequately.

3. For Q = 0.2, 0.3 Å, the 2-state and 3-state topological phases approach π, indicating that there is a JT CI close to the C atom ($\sim$0.6 Å away) in the direction away from O (see Figure 1.1). For Q = 1.0, 1.2, 1.4 and 2.1 Å, quantization is achieved through a three state calculation. Still they yield topological phases close to π suggesting that the circular contour surrounds the the same CI.

4. For Q = 2.2, 2.3 and 2.4 Å, a three state calculation is required to achieve quantization. The computed topological phases, in these three cases, are close to 2π. The results suggest that the contours chosen surround two JT CIs and the other CI lies in the range Q = [2.1, 2.2] Å.

5. Results of calculations carried out as per scheme 2 to ascertain the existence and location of a second CI suggest that there is one CI, $\sim$0.4 Å away from the non-revolving O atom.

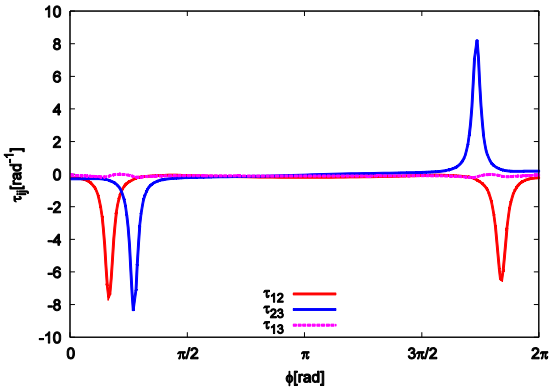

(a) Q = 0.2 Å (scheme 1)

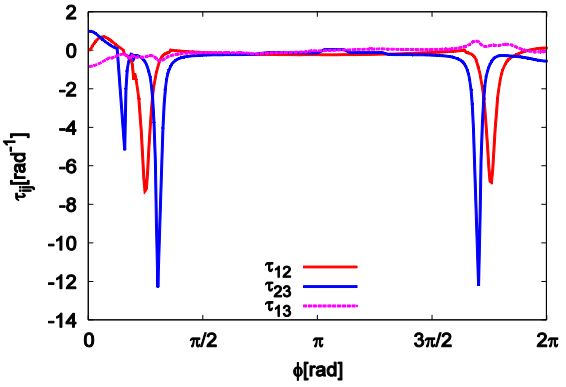

(b) Q = 0.3 Å (scheme 1)

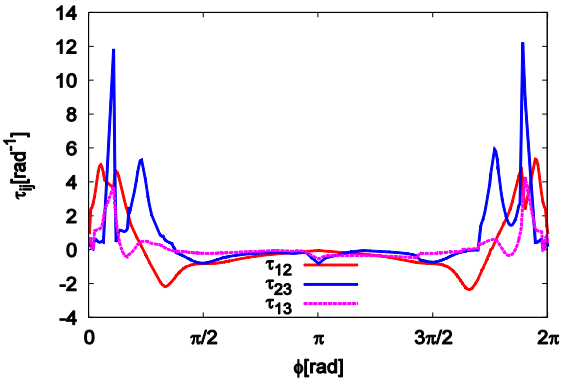

(c) Q = 1.0 Å (scheme 1)

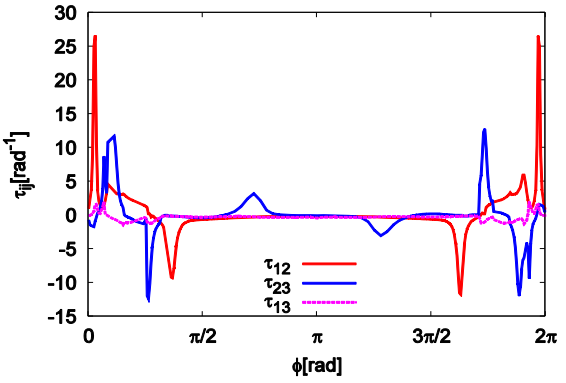

(d) Q = 1.2 Å (scheme 1)

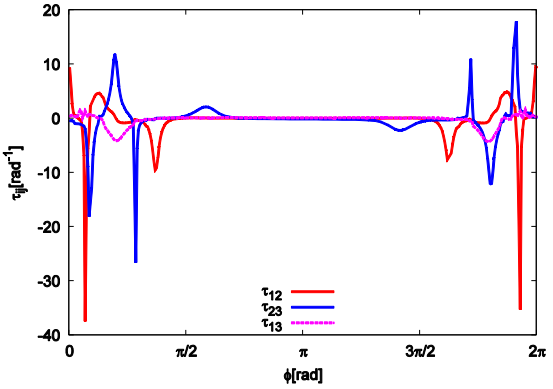

(e) Q = 1.4 Å (scheme 1)

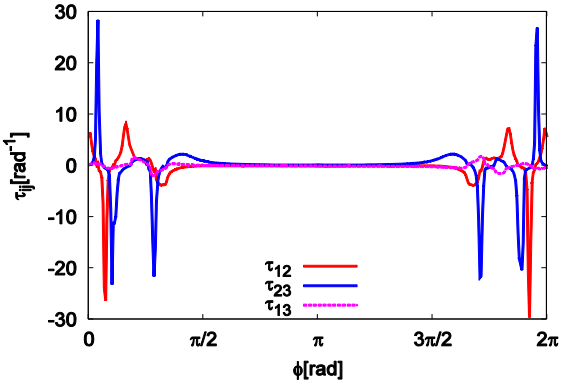

(f) Q = 2.1 Å (scheme 1)

Figure 1.3: NACTs (τ_{12}, τ_{13}, τ_{23}) plotted as a function of φ for different radii (Q) calculated with R2 = 0.6 Å

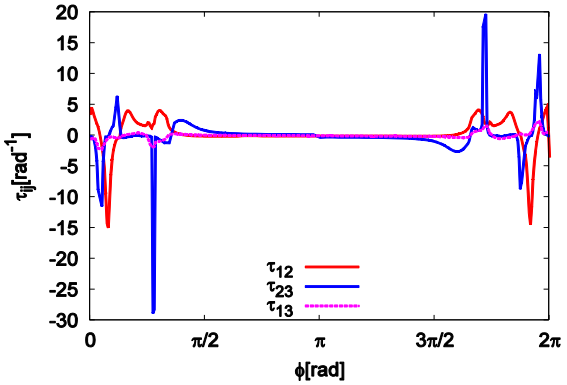

(a) Q = 2.2 Å (scheme 1)

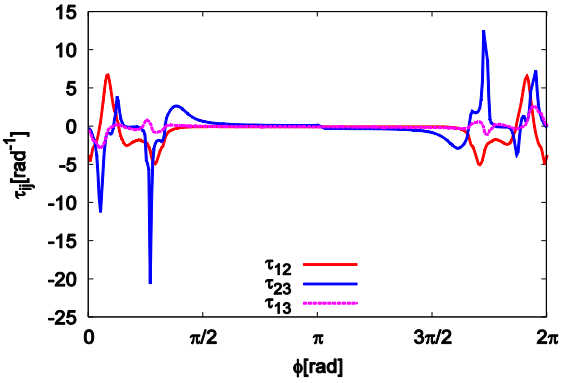

(b) Q = 2.3 Å (scheme 1)

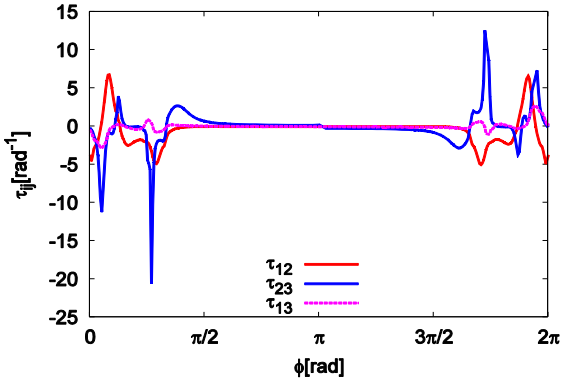

(c) Q = 2.4 Å (scheme 1)

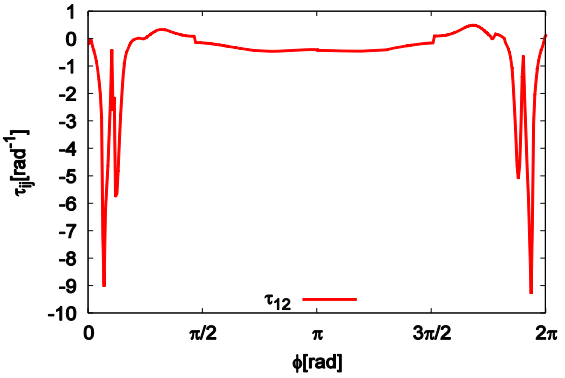

(d) Q = 0.4 Å (scheme 2)

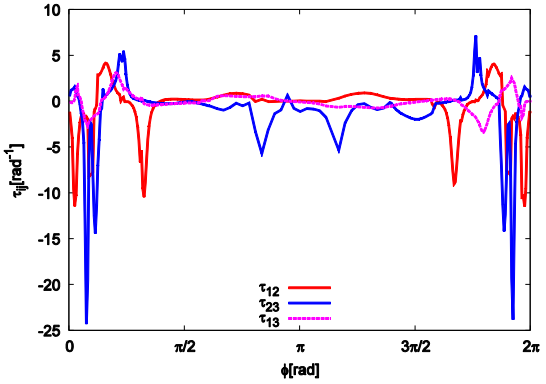

(e) Q = 1.2 Å (scheme 2)

Figure 1.4: NACTs (τ_{12}, τ_{13}, τ_{23}) plotted as a function of φ for different radii (Q) calculated with R2 = 0.6 Å

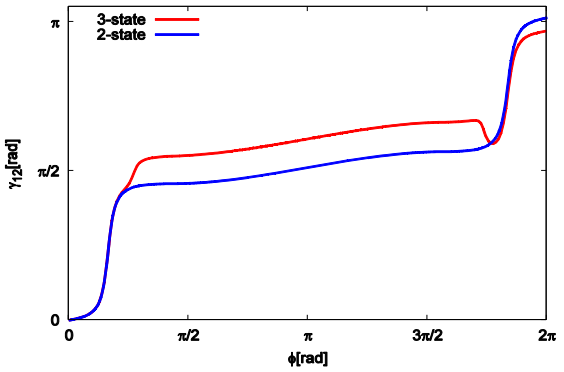

(a) Q = 0.2 Å (scheme 1)

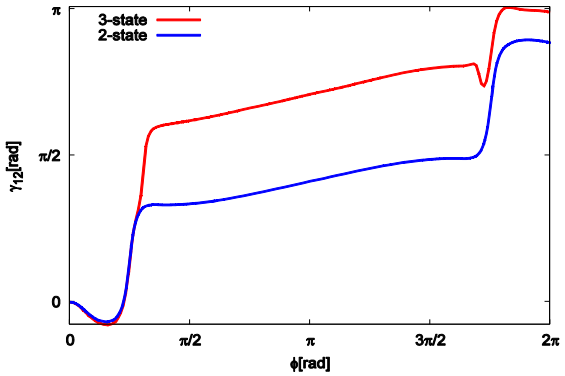

(b) Q = 0.3 Å (scheme 1)

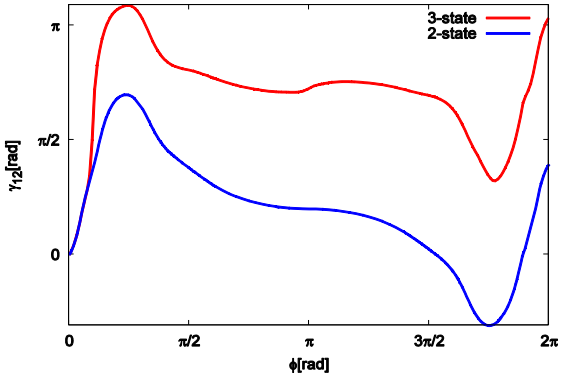

(c) Q = 1.0 Å (scheme 1)

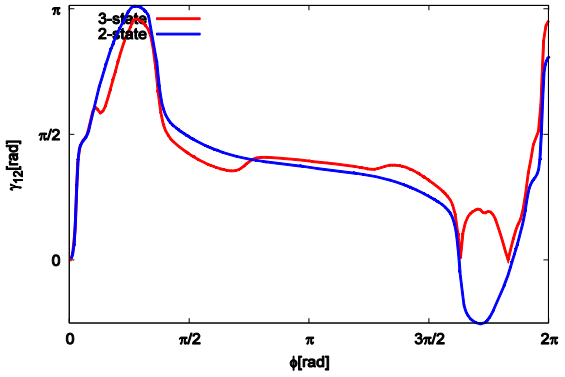

(d) Q = 1.2 Å (scheme 1)

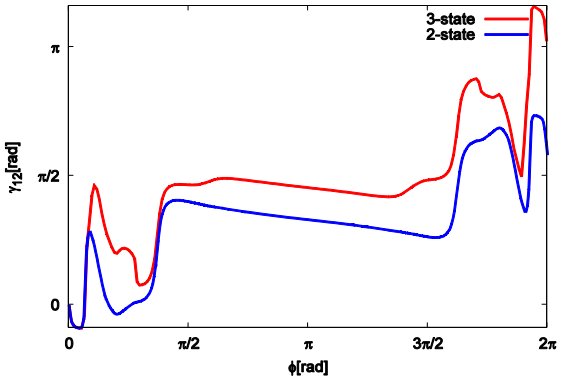

(e) Q = 1.4 Å (scheme 1)

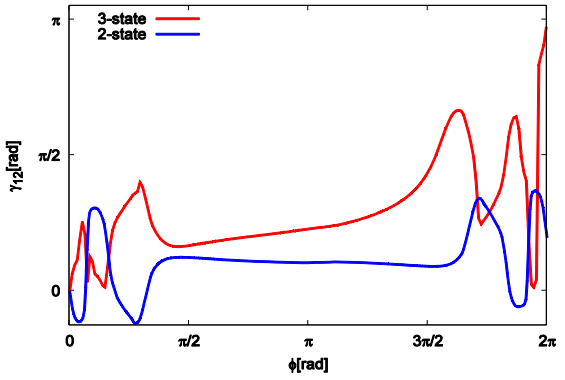

(f) Q = 2.1 Å (scheme 1)

Figure 1.5: 2-state and 3-state ADT angle γ_{12} plotted as a function of φ for different values of Q calculated with R2 = 0.6 Å

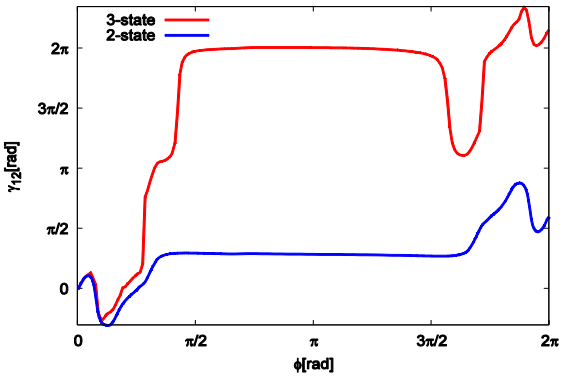

(a) Q = 2.2 Å (scheme 1)

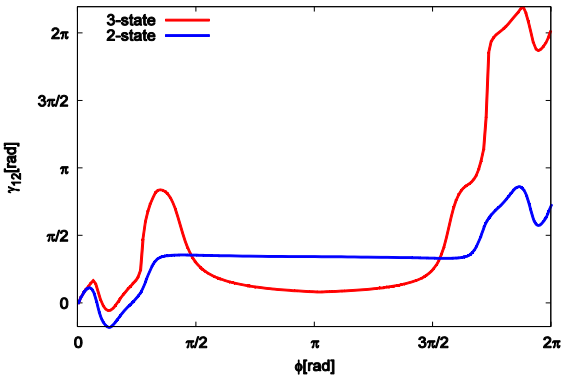

(b) Q = 2.3 Å (scheme 1)

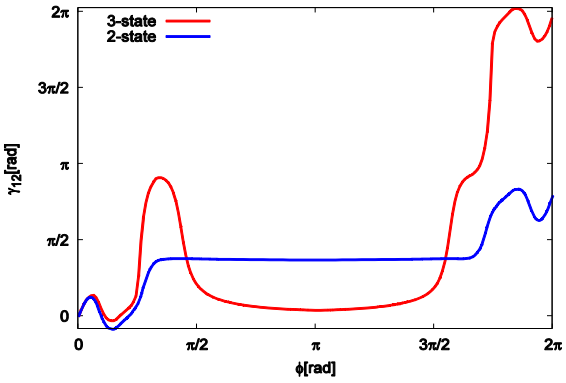

(c) Q = 2.4 Å (scheme 1)

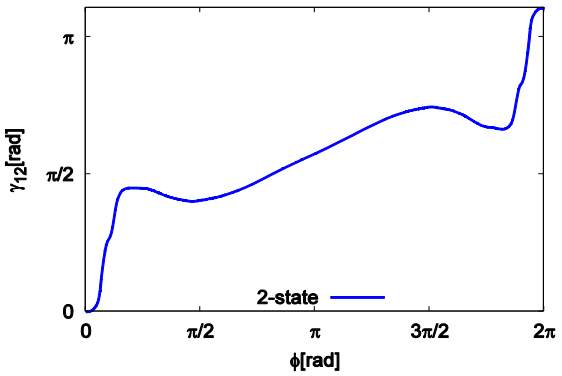

(d) Q = 0.4 Å (scheme 2)

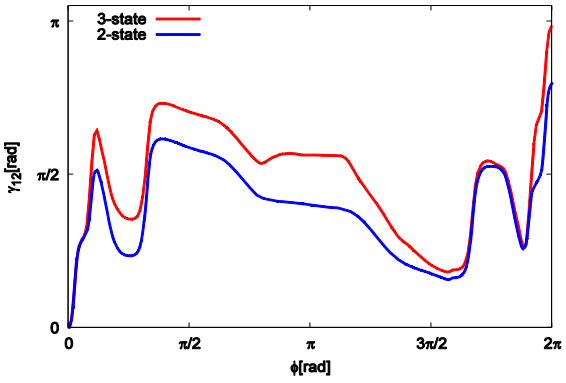

(e) Q = 1.2 Å (scheme 2)

Figure 1.6: 2-state and 3-state ADT angle γ_{12} plotted as a function of φ for different values of Q calculated with R2 = 0.6 Å

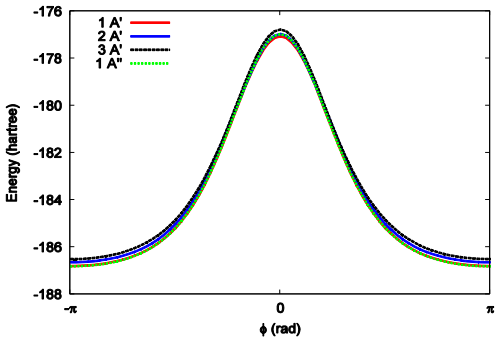

(a) Q = 0.2 Å (scheme 1)

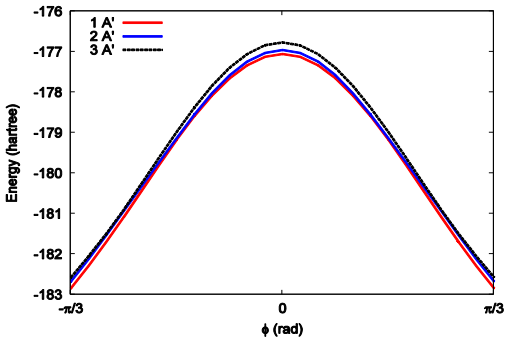

(b) Q = 0.2 Å (zoomed) (scheme 1)

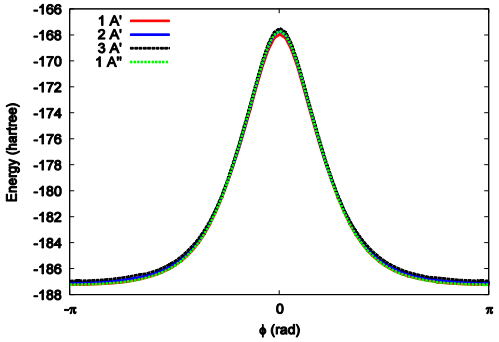

(c) Q = 0.3 Å (scheme 1)

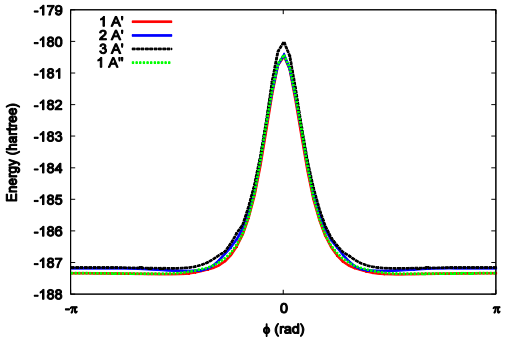

(d) Q = 1.2 Å (scheme 1)

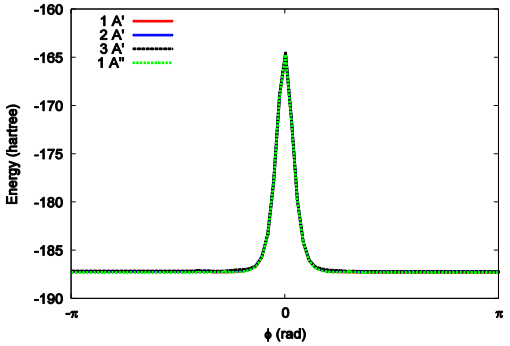

(e) Q = 2.1 Å (scheme 1)

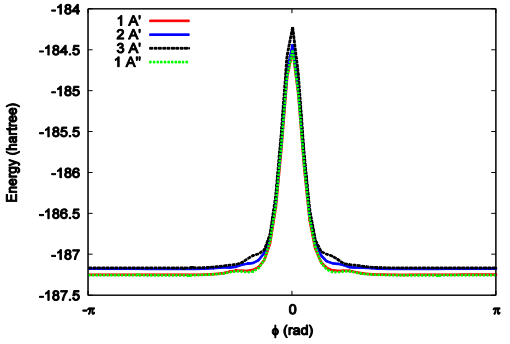

(f) Q = 2.4 Å (scheme 1)

Figure 1.7: Potential energy curves drawn as a function of φ for different values of Q, calculated with R2 = 0.6 Å using the MCSCF level of theory and the cc-pVTZ basis set.

Chapter 2

The Effect of Hydration on the Cation-π Interaction Between Benzene and Various Cations

2.1 Introduction

Non-covalent interactions, despite being weak, play a vital role in determining the physical and chemical properties of substances. There are several types of non-covalent interactions like hydrogen bond, stacking interaction, hydrophobic interaction, cation–π interaction, etc. They have been studied extensively to determine the extent of their influence in chemical and biological systems.[33–38] These interactions are used extensively to design novel materials and synthetic routes for efficient chemical processes.

The cation–π interaction is known to govern various chemical and biological phenomena like the stereochemistry in chemical processes, protein structure, transport across ion channels, molecular recognition and molecular aggregation.[39–49] Comprehensive reviews of the nature and the factors affecting the biological and chemical relevance of cation–π interaction have been provided by Ma and Dougherty,[39] Dougherty[40] and Mahadevi and Sastry.[41]

The cation-π interaction plays a significant role in size-selectivity of K-channel proteins which allow only K^+ to pass through and hinder the passage of Na^+.[44] Proteins assume shapes so as to maximize these non-covalent interactions. Various chemical processes have been reported wherein the cation–π interaction plays a significant role. Lakshminarasimhan et al.[50] have reported cation–π assisted selective geometric photoisomerization of *trans*-diphenylcyclopropane into *cis*-diphenylcyclopropane where cation–π interaction between the cation and benzene ring helps in bringing the two benzene moieties on the same side. Yamada et al.[51] have reported face selective addition of nucleophile in the benzene-pyridine complex where the cation-π interaction between benzene and pyridinium cation allows nucleophile to attack on benzene only from a particular side. Cation–π interaction is now extensively used to synthesize and design novel materials and chemical processes. Kim et al.[52] have reported the synthesis of ultrathin single-crystalline silver nanowire where Ag^+ ion is captured in calix[4]hydroquinones (CHQ) nanotube moieties through the cation–π interaction. Then Ag^+ is reduced to Ag atom through photochemical redox reaction to get crystalline silver nanowire.

A cation–π interaction is resulted when a neutral π–system interacts with a closed-shell cation. The cation–π interaction involves mainly an electrostatic interaction between a quadrupole (π–system) and an ion (cation). Therefore, it is essentially an ion-quadrupole interaction. Being of electrostatic origin, it is considered as one of the strongest non-covalent interactions.

The electrostatic component is not the sole component of cation–π interaction energy. Non-zero interaction energy between 1,3,5–trifluorobenzene (which has nearly zero quadrupole moment) and Na^+ ion shows that the cation–π interaction includes other intermolecular forces as well.[39,53] Other components of the cation–π interaction include a host of intermolecular interactions such as dispersion interaction, charge-dipole, charge-induced dipole, charge transfer, etc.[53] The electrostatic model proposed

by Dougherty and co-workers suggest that in the case of simple aromatics, 100% variation in the cation–π interaction energy can be predicted in terms of the electrostatic component alone and all other energy components fit into a constant parameter.[53]

There is experimental evidence for the cation–π interaction. Wu et al.[54] carried out a solid-state NMR study of alkali metal cations in their crystalline tetraphenylborate salts (M[BPh_4]), which contain the cation–π interaction, and tried to establish a relationship between the NMR spectral parameters of the alkali metal cations and ion binding environments. They found that alkali metal cations showed highly negative chemical shifts corresponding to the cation–π interaction.

The strength of the cation–π interaction depends on a variety of factors like the nature of the cation, nature of the π–system, solvation, heteroatom in the π–system and substituent in the π–system, etc. A cation with a higher charge density will interact more favourably with a π–system and will have a higher cation–π interaction strength. A cation which is coordination-wise less saturated will interact more favourably. Arenes (π–systems) with larger quadrupole moments are generally better at binding with cations as a larger quadrupole moment leads to a larger electrostatic interaction. The cations are known to have a preference for binding to a π-system with a higher π–electron content and aromaticity.[55]

The nature of the substituent(s) on the π–system also influences the strength of the interaction. Electron-withdrawing groups weaken the interaction, while electron-donating substituents strengthen the cation–π binding. Initially, π–polarization induced by the substituent(s) was thought to be a predominant factor for this substituent effect in the cation–π interaction as it "fits well with chemical intuition".[56] Later, Wheeler and Houk[57] showed that the substituent effects in the cation–π interactions do not arise *mainly* from the polarization of the aromatic π–system. Instead, this effect arises *primarily* through-space interaction between the cation and the sub-

stituent dipole .

Solvation is an important factor that governs the strength of the cation–π interaction. The nature of the solvent determines the absolute and relative strengths of interaction. Any intermediating solvent molecule will diminish the effect, because the cation-π interaction energy is partially offset by the loss of solvation energy. For a given cation-π system, the interaction energy decreases with an increase in solvent polarity.[58] It can be explained in terms of both solvation and coordinate saturation of cations. The cation–π interaction energy decreases with an increase in the solvation of the metal cation. The solvation energy and cation–π interaction balance is known to work in many chemical and biological phenomena. Ion-specificity in the K^+-ion channels is said to arise from the cation–π interaction.[44] The specificity is attributed to the sufficiently strong interaction between benzene and K^+ resulting in partial dehydration of the ion. Na^+ is unable to have such an interaction due to a larger hydration energy.[59]

The present work focuses on the effect of hydration on the cation–π interaction between various metal cations (Na^+, K^+, Mg^{+2}, Ca^{+2}, Al^{+3}) and benzene. It has been done by measuring the strength of the cation–π interaction of various metal cations in the dehydrated and partially hydrated states with benzene as the π–system and then comparing with the strength of interaction of the cations with water. Several computational and experimental works[59–64] have been directed towards studying the interaction of metal cations with benzene but the effect of solvation was not undertaken. Some of them do not discuss the solvent effect, but only calculate the cation–π interaction between benzene and alkali and alkaline-earth metal cations at different levels of theory and basis sets, to get an accurate cation-π interaction energy. Amicangelo and Armentrout[60] have calculated the absolute binding energies of alkali-metal cations with benzene and benzene dimer using the threshold collision-induced experiments and ab-initio theory at the MP2 level of theory and 6-31G* and 6-31G+** basis

sets. Cabarcos et al.[59] studied the solvation of Na^+ and K^+ by benzene and water using vibrational spectroscopy and proposed a mechanism for the size-selectivity of the K^+–ion channel proteins by cation–π interactions. They found that the K^+ ion can shed water molecules to get partly dehydrated from its first solvation shell to bind with an aromatic moiety but Na^+ prefers to interact with water molecules as it has a high hydration energy. Reddy et al.[61] studied the effect of sequential addition of water molecules (1 to 6) on the interaction between alkali and alkaline-earth metal cations and a benzene molecule and found that there is a reduction in the cation–π interaction energy as the number of water molecules increased around the cation and a sequential elongation in the cation-benzene bond distance. Nicholas et al.[62] carried out an ab-initio molecular orbital study of cation–π binding between the alkali-metal cations and benzene at various levels of theory . Feller et al.[63] estimated the complete basis set (CBS) limit for the cation-π bond strength for alkali-metal cations and benzene systems. Mishra et al.[64] have reported the interaction of benzene dimer and trimer with a host of cations at the MP2 level of theory and the using the 6-31G(*d,p*) basis set. They have reported the cation–π interaction energy values and π–cloud thickness values.

In the present work, the cations under study are alkali metal cations (Na^+, K^+), alkaline earth metal cations (Mg^{+2}, Ca^{+2}) and Al^{+3}. The total number of molecules around these cations are varied up to **three** with all possible combinations of benzene and water. The aim of the study is to find the qualitative trend in the interaction energies as the number of water and benzene molecules are varied around metal cations thereby observing the effect of hydration on cation–π interactions.

2.2 Methodology

The most basic and the most used *ab initio* electronic structure calculation is the Hartree-Fock (HF) method. But it has a major drawback in that it does not account for the instantaneous correlated motion of electrons. Thus the use of HF method to

study non-covalent interactions is limited. The second order Møller-Plesset perturbation theory (MP2), which takes account of electron correlation and it has been used to calculate the interaction energy. These methods (HF and MP2) have not been described in the thesis as they are elaborately discussed in standard textbooks.[65,66]

Interaction energy values were calculated using the *Supermolecule Method*. The interaction energy is calculated by subtracting the sum of energies of individual molecules (or atoms) from the energy of the complex.
Thus stabilization energy (ΔE_{stab}) of $M^{+q}B_nW_m$ is calculated as:

$$\Delta E_{stab} = E(M^{+q}B_nW_m) - [E(M^{+q}) + nE(B) + mE(W)], \tag{2.1}$$

where B, W and M^{+q} denote the benzene molecule, water molecule and the cation, respectively, while q denotes the charge on the cation. In this study, q varies from 1 to 3. Basis Set Superposition Error (BSSE) corrections were not calculated as the interaction energy values are expected to be large.
The π–cloud thickness has been calculated by subtracting the radii of different cations ($r(M^{+q})$) from the centre-of-mass separation between the cation and the benzene ring (r(Metal-Cent)) in the optimized geometry.

$$\pi - \text{cloud thickness} = r(\text{Metal-Cent}) - r(M^{+q}). \tag{2.2}$$

Charge densities for the cations have been calculated by dividing the total charge by the ionic volume. The formula for the Charge Density (CD) is given below for a cation M^{+q}:

$$\text{Charge Density} = \frac{q \times \text{e}}{\frac{4}{3}\pi r^3}, \tag{2.3}$$

where 'e' is the electronic charge equal to 1.6×10^{-19} C and r is the ionic radius of the cation.

2.3 Computational Details

Gaussian 09[67] suite of programs was used for the electronic structure calculations. Initially, geometry was optimized at the HF/6-31G(*d,p*) level and potential energy scan calculations were carried to locate the minimum. Later, all optimizations were carried out at the MP2 level of theory and using the 6-31G(*d,p*) basis set. Frequency calculations were then carried out to ascertain the nature of the resultant stationary point obtained. Most of the geometries reported in the thesis are characterized as minima with real frequencies. Other structures have very small and negligible imaginary frequencies.

2.4 Results and Discussion

2.4.1 Monomers

Table 2.1 lists the stabilization energy values for Al^{+3} ion, alkali and alkaline-earth metal cations with one water molecule. The stabilization energy values for Na^+, K^+, Mg^{+2}, Ca^{+2} and Al^{+3} with one water molecule come out to be -29.5, -21.7, -86.1, -57.7 and -198.6 kcal mol^{-1}, respectively. Corresponding optimized geometry is depicted in Figure 2.2a. The stabilization energy values for a benzene molecule with Na^+, K^+, Mg^{+2}, Ca^{+2} and Al^{+3} are -28.7, -19.8, -120.4, -71.1 and -356.3 kcal mol^{-1}, respectively. Corresponding optimized geometry is shown in Figure 2.2b. Stabilization energy values in the case of both benzene and water follow the trend of charge densities (Equation 2.3) i.e., the interaction energy value increases as the charge density of the cations increases. Stabilization energy values with benzene and water are the largest in case of Al^{+3}. It is because the Al^{+3} ion bears the highest charge density among the cations and has relatively a small size. Stabilization energy values are much larger for dications than for the monocations. Charge densities (abbreviated as CD in Table 2.1) are listed along with the stabilization energy values in Table 2.1.

From the results listed in Table 2.1, it is clear that Na^+ and K^+ favour interaction

Table 2.1: *Stabilization energy values*[a] *(in kcal mol*$^{-1}$*) for various cations with Water(W) and Benzene(B) at the MP2 level of theory and using the 6-31G(d,p) basis set.*

$\boldsymbol{M^{+q}}$	$\boldsymbol{CD}^{b,c}$	$\boldsymbol{\Delta E_{stab}(W)}$	$\boldsymbol{\Delta E_{stab}(B)}$
$\mathbf{Na}^{+}$	4.4	-29.5	-28.7
$\mathbf{K}^{+}$	1.6	-21.7	-19.8
$\mathbf{Mg}^{+2}$	27.8	-86.1	-120.4
$\mathbf{Ca}^{+2}$	7.8	-57.7	-71.1
$\mathbf{Al}^{+3}$	77.0	-198.6	-356.3

a: calculated using equation (2.1) in section 2.2. **b**: ***CD*** stands for charge density and values are given in $\times$ 10^{10} C/m^3. **c**: calculated using equation (2.3) in section 2.2.

with water over benzene by 0.8 and 1.9 kcal mol^{-1}, respectively. This is in contrast to what was observed experimentally by Kebarle et al.[68] They found that the K^+—B interaction is favoured over K^+—OH_2 in gas phase. Therefore, benzene cannot displace water in M^+—OH_2 complexes where M^+ is Na^+ or K^+. While the Mg^{+2} and Ca^{+2} ions interact more favourably with benzene over water by 34.3 and 13.4 kcal mol^{-1}, respectively. Therefore, benzene can displace the water molecule from the M^{+2}—OH_2 complexes, when M^{+2} is Mg^{+2} and Ca^{+2}. The trication Al^{+3} also prefers to interact strongly with benzene over water by 157.7 kcal mol^{-1}. This trend is also reflected in Figure 2.3a, which is a plot between the charge density of the cations and their stabilization energy values with water and benzene molecules.

Values of ΔE_{stab} plotted for different alkali metal cations interacting with the water lie lower than those for benzene. For the alkaline-earth metal cations and Al^{+3}, on the other hand values of ΔE_{stab} for benzene lie below those for water. Plots are given in Figure 2.1[a-b]

Optimized geometries for the adduct of water and benzene molecules with various cations are shown in Figures 2.2a and 2.2b. Some important features like π–cloud

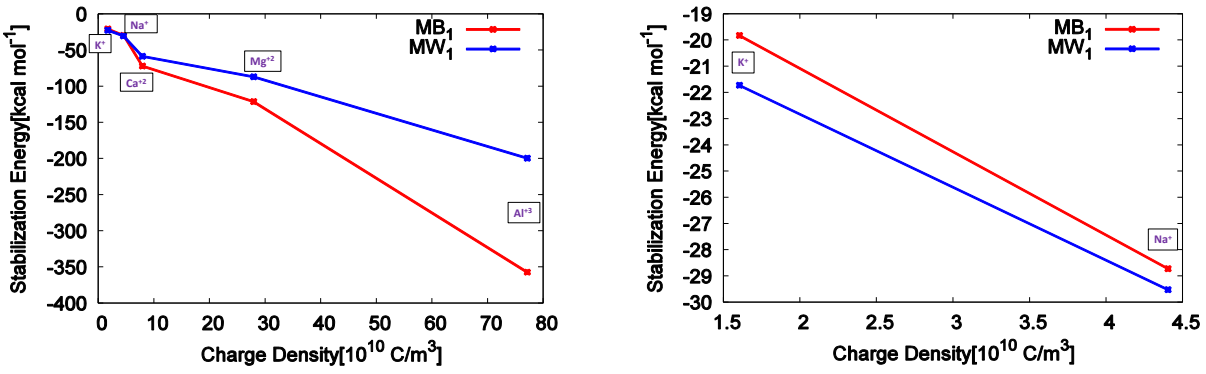

(a) Plot of ΔE_{stab} for MB_1 and MW_1 complexes.

(b) For MB_1 and MW_1, M = Na^+ and K^+ only

Figure 2.1: Plot of ΔE_{stab} for MB_1 and MW_1 complexes, where M^{+q} = Na^+, K^+, Mg^{+2}, Ca^{+2} and Al^{+3} at the MP2 level of theory and using the 6-31G(d,p) basis set.

thickness values applicable in the case of benzene as a partner and M^{+q}–O distances applicable in the case of water are listed in Table 2.2.

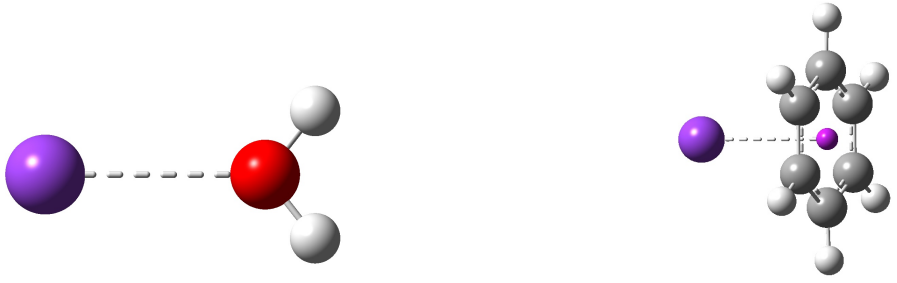

(a) M^{+q}—W

(b) M^{+q}—B

Figure 2.2: Optimized geometries for (a) water and (b) benzene interacting with M^{+q} = Na^+, K^+, Mg^{+2}, Ca^{+2} and Al^{+3} at the MP2 level of theory and using the 6-31G(d,p) basis set.

All geometries have been optimized at the MP2 level of theory using the 6-31G(d,p) basis set. All the geometries reported have been found to be minima with real frequencies.

Table 2.2: *π–cloud thickness values[a] and M^{+q}–O distances (in Å) for various cations with Water(W) and Benzene(B) at the MP2 level of theory using the 6-31G(d,p) basis set.*

M^{+q}	$r(M^{+q})$ [69,70]	M^{+q}–O Distance	M^{+q}-Cent Distance	π–cloud thickness[a]
Na^+	0.95	2.23	2.42	1.47
K^+	1.33	2.62	2.87	1.54
Mg^{+2}	0.65	1.95	1.98	1.33
Ca^{+2}	0.99	2.33	2.50	1.51
Al^{+3}	0.53	1.77	1.64	1.11

a: π–cloud thickness is calculated using equation (2.2) given in section 2.2.

The M^{+q}—O distance increases as the size of the cation increases. The M^{+q}—O distances for Na^+, K^+, Mg^{+2} Ca^{+2} and Al^{+3} in $M^{+q}—W$ complexes are 2.23, 2.62, 1.95, 2.33 and 1.77 Å, respectively.

In the case of $M^{+q}—B$ complexes, all cations in the optimized geometry are placed symmetrically above the C_6-axis of the benzene ring. The metal-centroid distance for Na^+, K^+, Mg^{+2} Ca^{+2} and Al^{+3} from benzene are 2.42, 2.87, 1.98, 2.50 and 1.64 Å, respectively. Therefore, it becomes clear that the metal cation–benzene centroid distance increases as the size of the metal-cation increases. In the case of Al^{+3}, the distance of the cation from the benzene centroid (1.64Å) is less than the distance from the O atom (1.77Å) of water. Clearly, cations with high charge densities interact with the π-system strongly. The π-cloud thickness values are computed to be 1.47, 1.54, 1.33, 1.51 and 1.11 Å for benzene monomer interacting with Na^+, K^+, Mg^{+2}, Ca^{+2} and Al^{+3}, respectively. Trend suggests that the π-cloud thickness value increases as the size of the metal-cation increases.

2.4.2 Dimers

The stabilization energy values of water dimer interacting with Na^+, K^+, Mg^{+2}, Ca^{+2} and Al^{+3} are computed to be -56.5, -41.4, -164.2, -111.1 and -369.6 kcal mol^{-1}, respectively. Optimized geometries of these systems are depicted in Figure 2.4a. The stabilization energy values in the case of water dimer are nearly double that of the water monomer interacting with different cations. Deviations from the additivity for Na^+, K^+, Mg^{+2}, Ca^{+2} and Al^{+3} are 2.5, 1.9, 8.0, 4.3 and 27.6 kcal mol^{-1}, respectively. The deviation is significant in the case of Mg^{+2} and Al^{+3}. The stabilization energy values for different cations with benzene dimer in a sandwiched geometry are listed in Table 2.3 and the corresponding optimized geometries are depicted in Figure 2.4c. The stabilization energy values for Na^+ and K^+ are computed to be -54.8 and -38.9 kcal mol^{-1}. The stabilization energy values for the Mg^{+2} and Ca^{+2} interacting with benzene dimer are computed to be -208.2 and -132.2 kcal mol^{-1} respectively. For Al^{+3} ion, it is -539.6 kcal mol^{-1}. It is clear that the stabilizing energy values for benzene dimer with divalent cations are far higher than those for monovalent cations. This may be attributed to higher charge density of the alkaline-earth metal cations in comparison to the alkali-metal cations. As stated earlier, cations with higher charge density interact more strongly with the π–system. Like in the case of water dimer, stabilization energy values for benzene dimer with various cations are found to be nearly double that for the benzene monomer, suggesting that the stabilization energy values are additive for π–cation–π interactions. For the benzene-water ***mixed dimer***, the stabilization energy values for Na^+, K^+, Mg^{+2}, Ca^{+2} and Al^{+3} are -55.1, 39.7, -190.1, -121.6 and 482.5 kcal mol^{-1}, respectively. The stabilization energy values for the mixed dimer are nearly the sum of the individual stabilization energy values for benzene and water. In all cases, the stabilization energy values increase as the charge density of the cations increases. The stabilization energy value is maximum for Al^{+3} for all the three cases (water dimer, benzene dimer and mixed dimer).

In the case of all the three dimers, the π-cation–π interactions are found to be

nearly additive. Deviations from additivity for Na^+, K^+, Mg^{+2}, Ca^{+2} and Al^{+3} are 2.6, 0.7, 31.6, 10.0 and 73.0 kcal mol^{-1}, respectively. Here again, the deviation is large for Mg^{+2} and Al^{+3}. As stated earlier, the cation–π interaction involves a host of interactions like electrostatic interaction, inductive interaction and dispersion interactions. Most dominant among these is the electrostatic interaction, which is strictly additive in nature. Therefore, the cation–π interaction is additive to a large extent.

As in the case of benzene and water monomers, Na^+ and K^+ prefer to interact with water dimer over benzene dimer by 1.7 and 2.5 kcal mol^{-1}. The Mg^{+2}, Ca^{+2} and Al^{+3} ions prefer to interact with benzene dimer over water dimer by 44.0, 21.1 and 170.0 kcal mol^{-1}, respectively. The stabilization energy values are far higher in the case of alkaline-earth metal cations and Al^{+3} ion than for alkali-metal cations.

Table 2.3: *Stabilization energy values[a] (in kcal mol^{-1}) for different cations with water dimer (W_2), benzene dimer (B_2) and, Mixed Dimer (B_1W_1) at the MP2 level of theory using the 6-31G(d,p) basis set.*

M^{+q}	CD^b	$\Delta E_{stab}(W_2)$	$\Delta E_{stab}(B_2)$	$\Delta E_{stab}(B_1W_1)$
Na^+	4.4	-56.5	-54.8	-55.1
K^+	1.6	-41.4	-38.9	-39.7
Mg^{+2}	27.8	-164.2	-208.2	-190.1
Ca^{+2}	7.8	-111.1	-132.2	-121.6
Al^{+3}	77.0	-369.6	-539.6	-482.5

a: calculated using equation (2.1) in section 2.2. **b**: *CD* stands for charge density and values are given in $\times$ 10^{10} C/m^3.

The stabilization energy values for the mixed dimer (B_1W_1) interacting with different cations lie in between the ΔE_{stab} values for water dimer and benzene dimer but the order is different for the alkali metal cations and the alkaline earth metal cations and Al^{+3} ion.

In the case of alkali cations, ΔE_{stab} values increase in the following order: $B_2 < B_1W_1 < W_2$. However, in the case of alkaline-earth-metal cations and Al^{+3} ion, the ΔE_{stab} values increase in the order: $W_2 < B_1W_1 < B_2$.

Plots of ΔE_{stab} values versus charge density of different cations for the all dimer cases are shown in Figures 2.3[a-b].

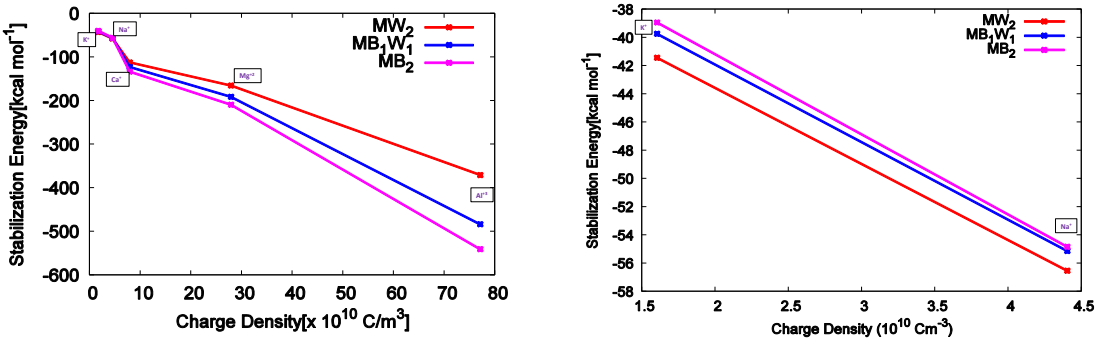

(a) Plot of ΔE_{stab} for For MB_mW_n, $m + n$=2 (b) For MB_mW_n $m + n$=2, M = Na^+ and K^+. complexes.

Figure 2.3: Plot of ΔE_{stab} for MB_mW_m, $m, n \geq 0$ and $n + m$=2, where M^{+q} = Na^+, K^+, Mg^{+2}, Ca^{+2} and Al^{+3} at the MP2 level of theory and using the 6-31G(d,p) basis set.

Optimized geometries for the dimers are shown in Figure 2.4[a-c]. Metal-centroid distance and π–cloud thickness values for M^{+q}—B_2 and M^{+q}—B_1W_1 complexes are listed in Table 2.4.

The geometries have been optimized at the MP2 level of theory and using the 6-31G(d,p) basis set. All geometries in the case of water dimer come out to be minima with real frequencies. It can be seen that the O atom of the water molecule is located 2.26, 2.64, 1.96, 2.35 and 1.77 Å away from Na^+, K^+, Mg^{+2}, Ca^{+2} and Al^{+3} cations, respectively. In all case cases except K^+, the O–M–O angle is 180°. The H–O—O–H dihedral angle is 90° to minimize the repulsion between two water molecules.

Table 2.4: *π–cloud thickness [a,b] for different cations with mixed dimer (B_1W_1) and Benzene dimer (B_2) at the MP2 level of theory using the 6-31G(d,p) basis set.*

M^{+q}	$r(M^{+q})^{a,69}$	M^{+q}-Cent $(B_2)^a$	π–thickness $(B_2)^a$	M^{+q}-Cent^a $(B_1W_1)^a$	π–thickness $(B_1W_1)^a$
Na^+	0.95	2.42	1.47	2.42	1.47
K^+	1.33	2.88	1.55	2.90	1.57
Mg^{+2}	0.65	2.05	1.40	2.01	1.36
Ca^{+2}	0.99	2.52	1.53	2.52	1.53
Al^{+3}	0.53	1.82	1.29	1.69	1.16

a: all values given are in Å. **b**: π–cloud thickness is calculated using equation (2.2) given in section 2.3.

Initial geometry given for optimization for benzene dimer was the eclipsed geometry with the cation sandwiched between two benzene moieties. A post-optimization frequency analysis indicates that some of the structures obtained are *first/second order saddle point* with very small and negligible imaginary frequency(ies). Upon optimization, the Na^+ and Mg^{+2} ions form stable geometry (minima) with real frequencies. Geometries of Ca^{+2} and Al^{+3} ions with benzene dimer turn out to be a first order saddle point with one small negligible imaginary frequency ($\sim$10 cm^{-1}). For K^+, the geometry with benzene dimer turns out to be a second-order saddle point with two small imaginary frequencies (12.23 cm^{-1} being the largest).

The metal cation-centroid distances in the optimized geometries of benzene dimer with Na^+, K^+, Mg^{+2}, Ca^{+2} and Al^{+3} ions are 2.42, 2.88, 2.05 2.52 and 1.82 Å, respectively (listed in Table 2.4). It is found that the cation-centroid distance of the benzene dimer are slightly increased (to the second decimal place), when compared to the benzene monomer which can be attributed to the steric adjustment of two benzene molecules around the cation. That is, benzene molecules move slightly apart to minimize the repulsion. In the optimized geometry, the two benzene molecules are

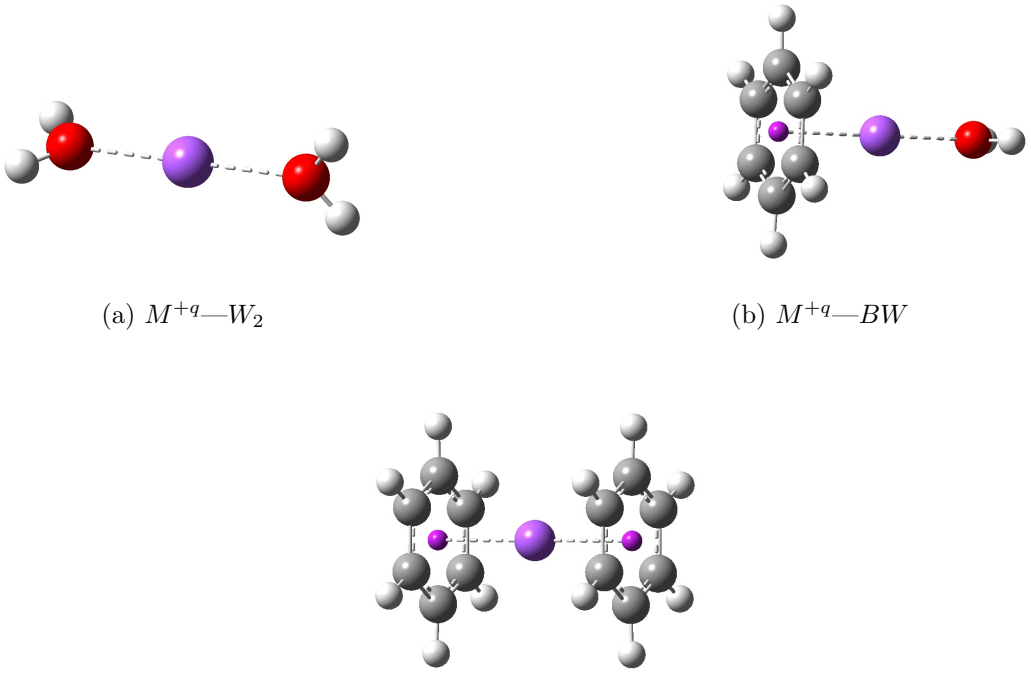

(a) M^{+q}—W_2

(b) M^{+q}—BW

(c) M^{+q}—B_2

Figure 2.4: Optimized geometries for (a) water dimer, (b) benzene-water mixed dimer and (c) benzene dimer with M^{+q} = Na^+, K^+, Mg^{+2}, Ca^{+2} and Al^{+3} at the MP2 level of theory and using the 6-31G(d,p) basis set.

eclipsed with respect to each other and the two benzene moieties have equal distance from the metal centre. In optimized geometries, B—M—B angle is 180°. Values of the π–cloud thickness in the case of the benzene dimer with Na^+, K^+, Mg^{+2}, Ca^{+2} and Al^{+3} ions are 1.47, 1.55, 1.40, 1.53 and 1.29 Å, respectively. As the metal-centroid distance is slightly enhanced in the case of benzene dimer, the π-thickness values also increase.

In MB_1W_1 complexes, the M—B and M—O bond lengths are nearly the same as in the case of MB_2 and MW_2. The $B(X)$—M—O bond angles vary in the range 170-180° for different cations. Optimized geometries are shown in Figure 2.4b. Optimized geometries for the mixed dimer for all the cations are characterized to be

minima except for K^+ for which the optimized geometry is found to be a second-order saddle point with the highest imaginary frequency being 9.7 cm^{-1}. For Mg^{+2} and Al^{+3} ions, the optimized geometry is linear, but for Na^+, K^+ and Ca^{+2} it is slightly bent ($\sim$170^o). The metal-benzene centroid distances in the mixed dimer complex for Na^+, K^+, Mg^{+2}, Ca^{+2} and Al^{+3} are 2.42, 2.90, 2.01, 2.52 and 1.69 Å, respectively and the corresponding π–thickness values are 1.47, 1.57, 1.36, 1.53 and 1.16 Å.

Summary: Alkali metal cations bind more strongly to water than benzene, their order being $B_2 < B_1W_1 < W_2$. The ΔE_{stab} value is larger for alkaline earth metal cations and Al^{+3} ion interacting with benzene than water, their order being $W_2 < B_1W_1 < B_2$. ΔE_{stab} values is the largest for Al^{+3}. The ΔE_{stab} increases with an increase in the charge density.

2.4.3 Trimers

The stabilization energy values for MB_mW_n, $m, n \geq 0$, m+n=3 are listed in Table 2.5.

The stabilization energy values for Na^+, K^+ and Ca^{+2} with the benzene trimer (B_3) are -70.2, -57.5 and -172.5 kcal mol^{-1}, respectively (see Table 2.5). Efforts to optimize the geometry for MB_3 for $M = Mg^{+2}$ and Al^{+3} were not successful. Optimized geometries in all other cases illustrated in Figure 2.7c. As expected, the stabilization energy values for dications are larger than those of monocations. In the case of benzene trimer, the ΔE_{stab} values for different cations are close to three times the value for benzene monomer. However, the deviation from additivity (16.6 and 1.9 kcal mol^{-1} for Na^+ and K^+, respectively) is larger for the trimer than for the dimer (2.6 and 1.9 kcal mol^{-1} for Na^+ and K^+, respectively) . ΔE_{stab} for Ca^{+2}—B_3 deviates considerably (30.8 kcal mol^{-1}) from the additivity property. Therefore, we can say that as the number of benzene molecules around the cation is increased, the deviation from additivity increases.

Table 2.5: *Stabilization energy values (in kcal mol^{-1}) for different cations with water trimer (W_3), benzene trimer (B_3) and, mixed trimers (B_1W_2, B_2W_1) at the MP2 level of theory using the 6-31G(d,p) basis set.*

M^{+q}	CD	$\Delta E_{stab}(B_3)$	$\Delta E_{stab}(B_2W_1)$	$\Delta E_{stab}(B_1W_2)$	$\Delta E_{stab}(W_3)$
Na^+	4.4	-70.2	-74.6	-76.7	-79.3
K^+	1.6	-57.5	-57.4	-57.8	-59.2
Mg^{+2}	27.8	NA	-243.3	-242.1	-229.4
Ca^{+2}	7.8	-172.5	-172.0	-166.3	-159.0
Al^{+3}	72.8	NA	-586.9	-565.7	-501.2

In the case of the mixed trimer B_2W_1, the ΔE_{stab} values for Na^+, K^+, Mg^{+2}, Ca^{+2} and Al^{+3} are found to be -74.6, -57.4, -243.3, -172.0 and -586.9 kcal mol^{-1}, respectively. Clearly, they increase with an increase in the charge density increase. The ΔE_{stab} values for this mixed trimer (B_2W_1) with different cations are significantly different from the sum of the individual stabilization energy values for benzene and water monomers with these cations. Only K^+ follows the additivity rule with a small deviation of 3.9 kcal mol^{-1}. All other cations have a deviation of more than $>$ 10 kcal mol^{-1}.

The stabilization energy values for B_1W_2 with Na^+, K^+, Mg^{+2}, Ca^{+2} and $Al^{+3}$are -76.7, -57.8, -242.1, -166.3 and -565.7 kcal mol^{-1}, respectively and are comparable to those for B_2W_1 (see Table 2.5).

For the water trimer, the stabilization energy values with Na^+, K^+, Mg^{+2}, Ca^{+2} and Al^{+3} are computed to be -79.3, -59.2, -229.4, -159.0 and -501.2 kcal mol^{-1}, respectively.

From the ΔE_{stab} data obtained for the trimers, it can be concluded that the alkali metal cations (Na^+ and K^+) bind more strongly to water than to benzene molecule. The stabilization energy values increase when benzene molecule is replaced sequentially with water in the cation-benzene trimer complex as can be seen from

the values listed in Table 2.6. Hydration $\{[B_3] \longrightarrow [B_2W_1]\}$ is favoured by Na^+ by -4.4 kcal mol^{-1}, but it is disfavoured by K^+ although by a small value of 0.1 kcal mol^{-1}. Further replacement of benzene with water$\{M^+[B_2W_1] \longrightarrow M^+[B_1W_2]\}$ is favoured by -2.1 and -0.4 kcal mol^{-1} for Na^+ and K^+, respectively. Further hydration $\{ M^+[B_1W_2] \longrightarrow M^+[W_3] \}$ is also favoured by -2.6 and -0.4 kcal mol^{-1}, respectively, for Na^+ and K^+.

Table 2.6: *Energy values (in kcal mol^{-1}) for conversion from one trimer to another at the MP2 level of theory using the 6-31G(d,p) basis set.*

Cation	$B_3 \rightarrow B_2W_1$	$B_2W_1 \rightarrow B_1W_2$	$B_1W_2 \rightarrow W_3$
Na^+	-4.4	-2.1	-2.6
K^+	0.1	-0.4	-0.4
Mg^{+2}	NA	1.2	12.6
Ca^{+2}	0.5	5.7	7.3
Al^{+3}	NA	21.2	64.5

The trend is reversed for alkaline-earth metal cations. They prefer to bind with benzene over water. For $M^{+2}[W_3] \longrightarrow M^{+2}[B_1W_2]$ conversion, the conversion energy values are -12.6 and -7.3 kcal mol^{-1}, for Mg^{+2} and Ca^{+2}, respectively. Further replacement of water by benzene $\{[B_1W_2] \longrightarrow [B_2W_1]\}$ is also favoured for Mg^{+2} and Ca^{+2} by -1.2 and -5.7 kcal mol^{-1}, respectively. For the process $Ca^{+2}[B_2W_1] \longrightarrow Ca^{+2}[B_3]$, the conversion energy is -0.5 kcal mol^{-1}.

The trication Al^{+3} follows the trend of alkaline-earth metal cations and favours binding with benzene over water. The first and second replacement of water by benzene is favoured by -64.5 and -21.2 kcal mol^{-1}, respectively.

Plot for ΔE_{stab} versus cation charge density are shown for trimers interacting with different cations are shown in Figure 2.5[a-b].

All the trimer geometries around the metal cations have been optimized at the

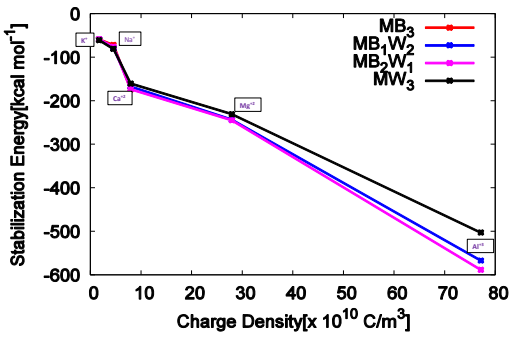

(a) Plot of ΔE_{stab} for metal cation-trimer complexes.

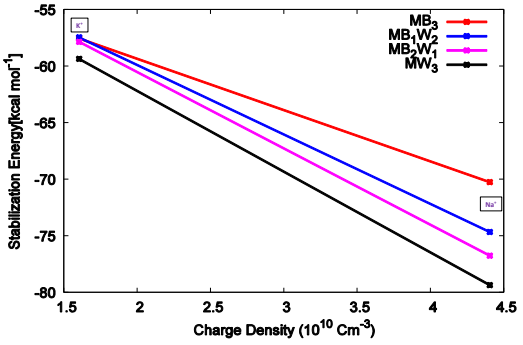

(b) ΔE_{stab} for trimer complexes for $M = \mathrm{Na}^+$ and K^+ only

Figure 2.5: Plot of ΔE_{stab} for MB_mW_n, $n, m \geq 0$ and $m+n=3$, interacting with M^{+q} = Na^+, K^+, Mg^{+2}, Ca^{+2} and Al^{+3} at the MP2 level of theory and using the 6-31G(*d,p*) basis set.

MP2 level of theory with the 6-31G(*d,p*) basis set. For $M^{+q}[B_3]$, the initial geometry was benzene molecule facing the cation with the centres of three benzenes arranged in a trigonal planar fashion thus forming a cavity of three benzene rings with the cation encapsulated in it. A frequency analysis for the optimized geometry shows that all the optimized benzene trimer geometries with different cations are minima with all real frequencies. The optimized geometries for the benzene trimer are shown in Figure 2.7c. For $M^{+q}B_3$, all the three benzene rings are equidistant from the central cation. The cation-centroid distances for $M^{+q}[B_3]$ for Na^+, K^+ and Ca^{+2} are computed to be 2.66, 2.91 and 2.65 Å, respectively. The angles between the benzene centres measured from the cation come out to be $\sim 120^o$. Nearby H atoms of benzene rings avoid each other by changing the angles to minimize the repulsion (see Figure 2.7c). The π-thickness values in case of the benzene trimer with Na^+, K^+ and Ca^{+2} are calculated to be 1.71, 1.58 and 1.66 Å, respectively. It should be noted that the smallest metal cation-centroid distance has been used to calculate the π–cloud thickness value when two benzene molecules are located at different distances from the cation.

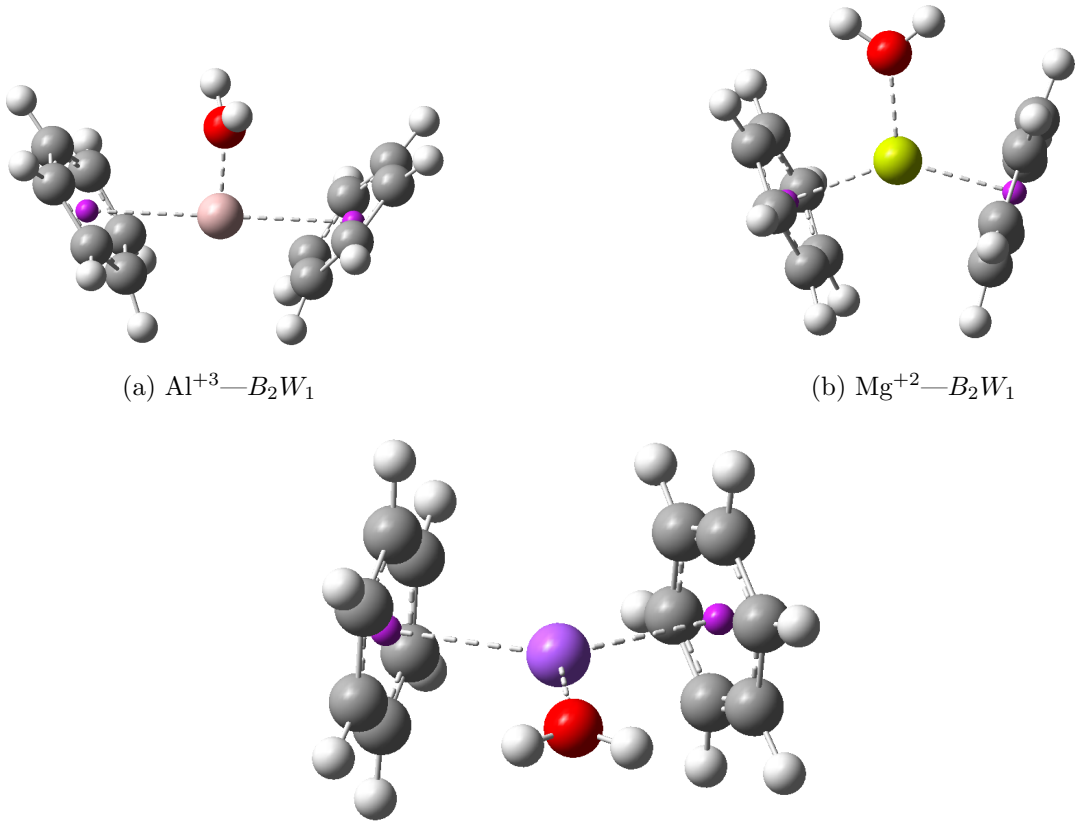

(a) Al^{+3}—B_2W_1 (b) Mg^{+2}—B_2W_1

(c) M^{+q}—B_2W_1

Figure 2.6: Optimized geometries of (a) Al^{+3}, (b) Mg^{+2} and (c) M^{+q} = Na^+, K^+, and Ca^{+2} for B_2W_1 at the MP2 level of theory and using the 6-31G(d,p) basis set.

In the case of the mixed trimer B_2W_1, all geometries reported correspond to minima with real frequencies. The metal-centroid distance for B_2W_1 with Na^+, K^+, Mg^{+2}, Ca^{+2} and Al^{+3} is computed to be 2.52, 2.91, 2.22, 2.57 and 2.58 Å , respectively. Large value of the metal-centroid distance for Al^{+3} is because both the benzenes are tilted towards the cation on one side and cation is not at right angle to the plane of benzene rings at their centres (see Figure 2.6a). Distances of different carbon atoms of benzene molecules from Al^{+3} ion vary in the range from 2.14-3.50 Å. Benzene molecules are also slightly tilted in the cases of the Mg^{+2}, with the Mg^{+2}—C distance varying in the range 2.56-2.66 Å (see Figure 2.6b). In all other cases (Na^+, K^+, Ca^{+2}), the M^{+q}—C distance remains nearly the same [maximum variation ∼0.04 Å] (see Figure

2.6c). The π-cloud thickness values for B_2W_1 with Na^+, K^+, Mg^{+2}, Ca^{+2} and Al^{+3} are calculated to be 1.57, 1.57, 1.57, 1.58 and 2.05 Å , respectively.

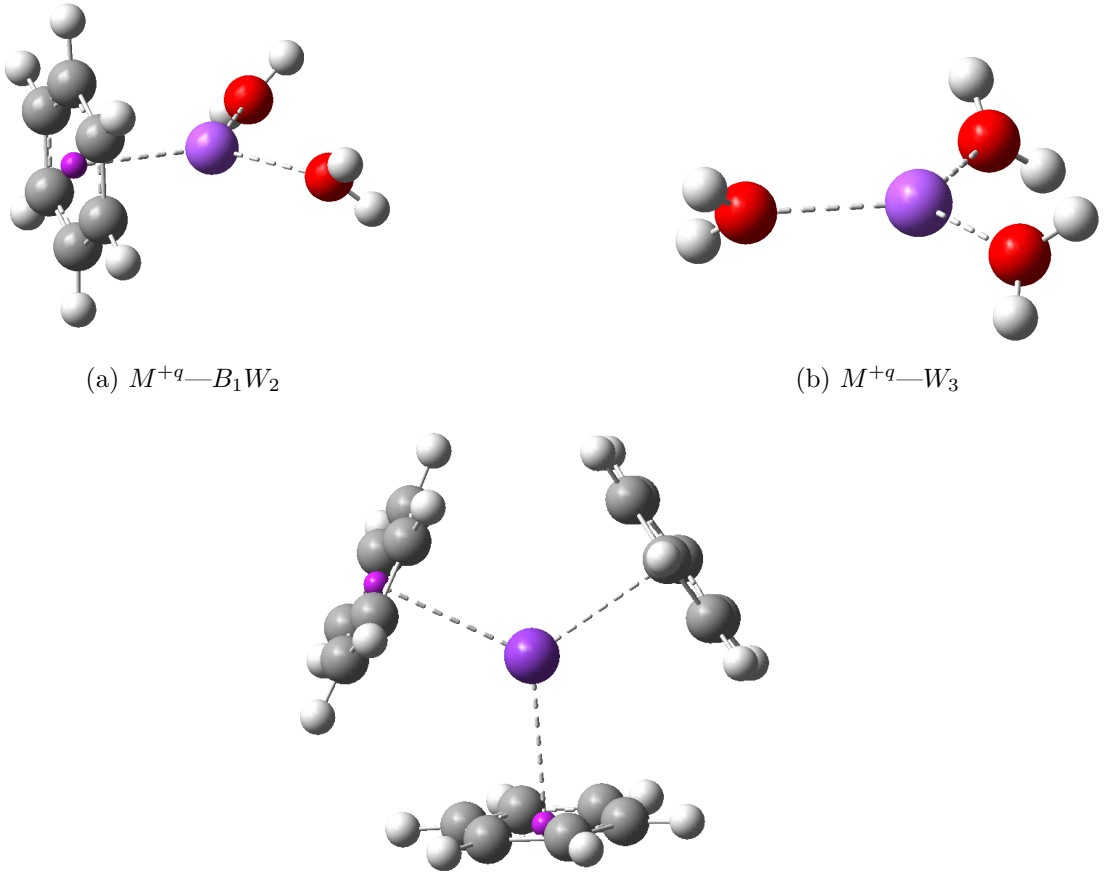

(a) M^{+q}—B_1W_2 (b) M^{+q}—W_3

(c) M^{+q}—B_3

Figure 2.7: Optimized geometries (a) for MB_1W_2, (b) MW_3 and (c) MB_3 with M = Na^+, K^+, Mg^{+2}, Ca^{+2} and Al^{+3} at the MP2 level of theory and using the 6-31G(*d,p*) basis set.

For the mixed dimer MB_1W_2, all the optimized geometries reported in Figure 2.7a are found to be as first-order saddle points except the Mg^{+2} and Al^{+3}. The smallest imaginary frequency for Na^+, K^+, and Ca^{+2} are -4.5, -2.1, and -3.7 cm^{-1}, respectively. The cation-centroid distance for B_1W_2 with Na^+, K^+, Mg^{+2}, Ca^{+2} and Al^{+3} is found to be 2.50, 2.92, 2.09, and 2.55 Å, respectively. The M^{+q}—O distance for both water molecules are the same and for Na^+, K^+, Mg^{+2}, Ca^{+2} and Al^{+3} ions it is found to

be 2.28, 2.66, 2.01, 2.37 and 1.79 Å, respectively. The π–cloud thickness values for B in MB_1W_2 with M = Na^+, K^+, Mg^{+2}, Ca^{+2} and Al^{+3} is computed to be 1.55, 1.59, 1.44, 1.56 and 1.26 Å , respectively.

Table 2.7: *π–cloud thickness [a] (in Å) for different cations in MB_1W_2, MB_2W_1 and MB_3 at the MP2 level of theory using the 6-31G(d,p) basis set.*

Property	$\mathbf{Na^+}$	$\mathbf{K^+}$	$\mathbf{Mg^{+2}}$	$\mathbf{Ca^{+2}}$	$\mathbf{Al^{+3}}$
$\mathbf{r(M^{+q})}$	0.95	1.33	0.65	0.99	0.53
$\mathbf{M^{+q}}$**-Cent**^{a} $(\mathbf{B_3})$	2.54	2.91	NA	2.65	NA
π–**thickness** $(\mathbf{B_3})$	1.59	1.58	NA	1.66	NA
$\mathbf{M^{+q}}$**-Cent**^{a} $(\mathbf{B_2W_1})$	2.54	2.91	2.22	2.57	2.58
π–**thickness** $(\mathbf{B_2W_1})$	1.58	1.58	1.57	1.58	2.05
$\mathbf{M^{+q}}$**-Cent**^{a} $(\mathbf{B_1W_2})$	2.50	2.92	2.09	2.55	1.79
π–**thickness** $(\mathbf{B_1W_2})$	1.55	1.59	1.44	1.56	1.26

a: Smaller metal cation-centroid distance is used to calculate the π–thickness whenever two benzene are located at different distances from the cation.

For MW_3, all geometries reported in Figure 2.7b are characterized as minima with real frequencies. The M^{+q}—O distance for M = Na^+, K^+, Mg^{+2}, Ca^{+2} and Al^{+3} is found to be 2.29, 2.66, 1.99, 2.37 and 1.81 Å, respectively. The angles between the water molecules measured from the cation come out to be $\sim$120^o. The H atoms in water molecule are suitably titled to minimize repulsion.

Plot of ΔE_{stab} against different complexes in Figure 2.8 summarizes all the results for different cations.

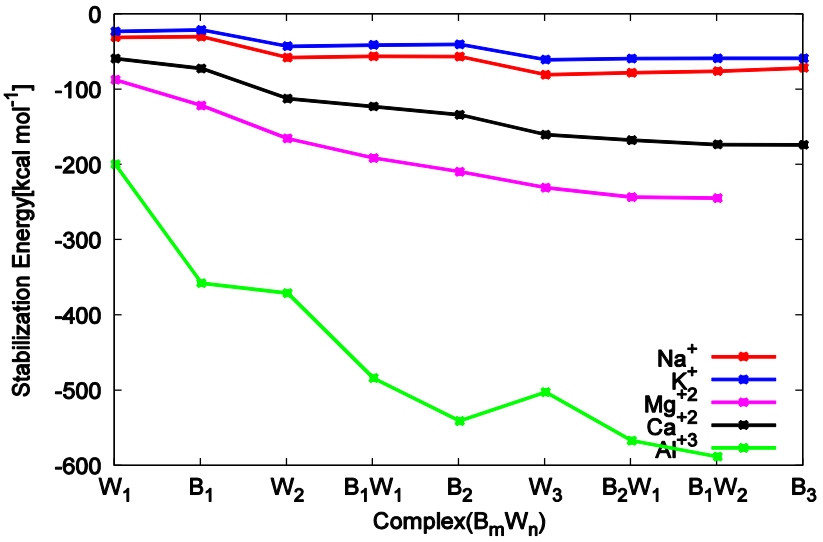

Figure 2.8: Plot of ΔE_{stab} against B_mW_n, $0 \leq n, m \leq 3$ for Na^+, K^+, Mg^{+2}, Ca^{+2} and Al^{+3} ions at the MP2 level of theory and using the 6-31G(d,p) basis set.

2.5 Summary and Conclusion

Ab-initio calculations were carried to study the effect of hydration on cation–π interaction between different alkali metal and alkaline earth metal cations and Al^{+3} and benzene at the MP2 level of theory using the 6-31G(d,p) basis set. The following conclusions can be drawn:

(i) The alkali metal cations prefer to bind with a single molecule of water over benzene, though the energy difference is small. The alkaline-earth metal cations and Al^{+3} ion, on the other hand, bind more strongly with the benzene than water.

(ii) In the case of MB_2, MB_1W_1, MW_2, ΔE_{stab} values follow the trend $B_2 < B_1W_1 < W_2$ for Na^+ and K^+, and $W_2 < B_1W_1 < B_2$ for Mg^{+2}, Ca^{+2} and Al^{+3} ions.

(iii) In case of the trimer, ΔE_{stab} value follow the trend $B_3 < B_2W_1 < B_1W_2 < W_3$, for Na^+ and K^+, and $W_3 < B_1W_2 < B_2W_1 < B_3$, for Mg^{+2}, Ca^{+2} and Al^{+3} ions.

(iv) The stabilization energy values for all systems (monomer, dimer and trimer) vary in the following order: $K^+ < Na^+ < Ca^{+2} < Mg^{+2} < Al^{+3}$ which is the order of charge density.

(v) The π–thickness value for benzene varies in the range $\sim$1.10-2.05 Å.

(vi) The stabilization energy values for the dimers/trimers are found to be nearly two/three times that of the monomer case. Deviations from additivity are larger for cations having higher charge densities and as the number of B/W molecules increases.

Bibliography

[1] Born, M.; Oppenheimer, J. R. *Ann. Phys. (Leipzig)* **1927**, *84*, 457.

[2] Born, M.; Huang, K. *Dynamical Theory of Crystal Lattices*; Oxford University Press: New York, 1954; Chapter IV.

[3] Longuet-Higgins, H. *Adv. Spectrosc.* **1961**, *2*, 429.

[4] Hellmann, H. *Einfuhrung in die Quantenchemie* **1937**, Deuticke, Leipzig.

[5] Feynman, R. P. *Phys. Rev.* **1940**, *56*, 340.

[6] Epstein, S. T. *Am. J. Phys.* **1954**, *22*, 613.

[7] Singh, S. B.; Singh, C. A. *Am. J. Phys.* **1989**, *57*, 894.

[8] Baer, M. *Chem. Phys. Lett.* **1975**, *35*, 112.

[9] Baer, R. *J. Chem. Phys.* **2002**, *117*, 7405.

[10] Baer, M. *Phys. Rep.* **2002**, *358*, 75.

[11] Hobey, W. D.; McLachlan, A. D. *J. Chem. Phys.* **1960**, *33*, 1695.

[12] Baer, M. *Molec. Phys.* **1980**, *40*, 1011.

[13] Pacher, T.; Cederbaum, L. S.; Köppel, H. *Adv. Chem. Phys.* **1993**, *84*, 293.

[14] Baer, M. *J. Phys. Chem. A* **2000**, *104*, 3181.

[15] Smith, F. T. *Phys. Rev.* **1969**, *179*, 111.

[16] Baer, M. In *Theory of Chemical Reaction Dynamics*; Baer, M., Ed.; CRC Press: Boca Raton, FL, 1985; Vol. II; Chapter 4.

[17] Baer, M.; Alijah, A. *Chem. Phys. Lett.* **2000**, *319*, 489.

[18] Baer, M.; Lin, S. H.; Alijah, A.; Adhikari, S.; Billing, G. D. *Phys. Rev. A* **2000**, *62*, 032506–1.

[19] Baer, M.; V értesi, T.; Halàsz, G. J.; Vibók, A.; Suhai, S. *Faraday Disc.* **2004**, *127*, 337.

[20] Werner, H.-J.; Knowles, P. J.; Knizia, G.; Manby, F. R.; Schutz, M.; et al., MOLPRO version 2010.1. 2010.

[21] Baer, M.; Mebel, A. M.; Billing, G. D. *Int. J. Quant. Chem.* **2002**, *90*, 1577.

[22] Halàsz, G. J.; Vibók, A.; Baer, R.; Baer, M. *J. Chem. Phys.* **2006**, *125*, 094102.

[23] Top, Z. H.; Baer, M. *J. Chem. Phys.* **1977**, *66*, 1363.

[24] Alijah, A.; Baer, M. *J. Phys. Chem. A* **2000**, *104*, 389.

[25] Baer, M. *Beyond Born-Oppenheimer: Electronic Non-adiabatic Coupling Terms and Conical Intersections*; Wiley & Sons Inc.: Hoboken NJ, 2006; section 5.5.3.

[26] Sarkar, B.; Adhikari, S. *J. Chem. Phys.* **2006**, *124*, 074101.

[27] Sarkar, B.; Adhikari, S. *J. Phys. Chem. A* **2008**, *112*, 9868.

[28] Das, A.; Mukhopadhyaya, D. *J. Phys. Chem. A* **2012**, *116*, 1774.

[29] Longuet-Higgins, H. C.; Opik, U.; Pryce, M. H. L.; Sack, R. A. *Proc. Roy. Soc. Lond. A* **1958**, *244*, 1.

[30] Herzberg, G.; Longuet-Higgins, H. C. *Disc. Faraday Soc.* **1963**, *35*, 77.

[31] Longuet-Higgins, H. C. *Proc. Roy. Soc. Lond. A* **1975**, *344*, 147.

[32] Kendall, R. A.; Dunning Jr, T. H.; Harrison, R. J. *J. Chem. Phys.* **1992**, *96*, 6796.

[33] Desiraju, G. R. *Acc. Chem. Res.* **2002**, *35*, 565.

[34] Meyer, E. A.; Castellano, R. K.; Diederich, F. *Angew. Chem. Int. Ed.* **2003**, *42*, 1210.

[35] Salonen, L. M.; Ellermann, M.; Diederich, F. *Angew. Chem. Int. Ed.* **2011**, *50*, 4808.

[36] Steiner, T. *Angew. Chem. Int. Ed.* **2002**, *41*, 48.

[37] Joseph, J.; Jemmis, E. D. *J. Am. Chem. Soc.* **2007**, *129*, 4620.

[38] Parthasarathi, R.; Subramanian, V.; Sathyamurthy, N. *J. Phys. Chem. A* **2006**, *110*, 3349.

[39] Ma, J. C.; Dougherty, D. A. *Chem. Rev.* **1997**, *97*, 1303.

[40] Dougherty, D. A. *Acc. Chem. Res.* **2013**, *46*, 885–893.

[41] Mahadevi, A. S.; Sastry, G. N. *Chem. Rev.* **2013**, *113*, 2100–2138.

[42] Dougherty, D. *Science* **1996**, *271*, 163.

[43] Gallivan, J. P.; Dougherty, D. *Proc. Natn. Acad. Sci.* **1999**, *96*, 9459.

[44] Kumpf, R.; Dougherty, D. *Science* **1993**, *261*, 1708.

[45] Zhu, W. L.; Tan, X. J.; Puah, C. M. t. *J. Phys. Chem. A* **2000**, *104*, 9573.

[46] Tan, X. J.; Jiang, H. L.; Zhu, W. L. t. *J. Chem. Soc., Perkin Trans.* **1999**, *1*, 107.

[47] Gokel, G. W.; De Wall, S. L.; Meadows, E. S. *Eur. J. Org. Chem.* **2000**, *17*, 2967.

[48] DeVos, A. M.; Ultsch, M.; Kossiakoff, A. A. *Science* **1992**, *255*, 306.

[49] Mitchell, J. B.; Nandi, C. L.; McDonanld, I. K. t. *J. Molec. Biol.* **1994**, *239*, 315.

[50] Lakshminarasimhan, P.; Sunoj, R. B.; Chandrasekhar, J.; Ramamurthy, V. *J. Am. Chem. Soc.* **2000**, *122*, 4815.

[51] Yamada, S.; Morita, C. *J. Am. Chem. Soc.* **2002**, *124*, 8184.

[52] Hong, B. H.; Bae, S. C.; Lee, C. W.; Jeong, S.; Kim, K. S. *Science* **2001**, *294*, 348.

[53] Mecozzi, S.; West, J., A. P.; Dougherty, D. A. *J. Am. Chem. Soc.* **1996**, *93*, 2307.

[54] Wu, G.; Terskikh, V. *J. Phys. Chem. A* **2008**, *112*, 10359.

[55] Lee, J. S.; Krasnokutski, S. A.; Yang, D. *J. Chem. Phys.* **2011**, *134*, 024301.

[56] Hunter, C. A.; Low, C. M. R.; Rotger, C.; Vinter, J. G.; Zonta, C. *Proc. Natn. Acad. Sci.* **2002**, *99*, 4873.

[57] Wheeler, S. E.; Houk, K. N. *J. Am. Chem. Soc.* **2009**, *131*, 3126.

[58] Gallivan, J. P.; Dougherty, D. A. *J. Am. Chem. Soc.* **2000**, *122*, 870.

[59] Cabarcos, O. M.; Weinheimer, C. J.; Lisy, J. M. *J. Chem. Phys.* **1999**, *110*, 2307.

[60] Amicangelo, J. C.; Armentrout, P. B. *J. Phys. Chem. A* **2000**, *104*, 11420.

[61] Reddy, A. S.; Zipse, H.; Sastry, G. N. *J. Phys. Chem. B* **2007**, *111*, 11546.

[62] Nicholas, J. B.; Hay, B. P.; Dixon, D. A. *J. Phys. Chem. A* **1999**, *103*, 1394.

[63] Feller, D.; Dixon, D. A.; Nicholas, J. B. *J. Phys. Chem. A* **2000**, *104*, 11414.

[64] Mishra, B. K.; Bajpai, V. K.; Ramanathan, V.; Gadre, S. R.; Sathyamurthy, N. *Mol. Phys.* **2008**, *106*, 1557.

[65] Levine, I. N. *Quantum Chemistry*, sixth ed.; PHI Learning Ltd.: New Delhi, 2010.

[66] Szabo, A.; Ostlund, N. S. *Modern Quantum Chemistry*; Dover Publications, Inc.: Mineola, New York, 1996.

[67] Frisch, M. J. et al. *Gaussian 09*; Gaussian Inc.: Pittsburg, PA., For furher information, see: http://www.Gaussian.com/index.htm.

[68] Sunner, J.; Nishizawa, K.; Kebarle, P. *J. Phys. Chem.* **1981**, *85*, 1814.

[69] Gadre, S. R.; Sen, K. D. *J. Chem. Phys.* **1993**, *99*, 3149.

[70] Wells, A. F. *Structural Inorganic Chemistry*, 4th ed.; Clarendon Press - Oxford, Oxford University Press: Ely House, London, 1975; Page 259.